bioRχiv

New neural-inspired controller generalises modularity over lower limb tasks through internal models

David Muñoz[a,b,*], Dónal Holland[c], and Giacomo Severini[a,b]
[a]School of Electrical and Electronic Engineering, University College Dublin, Dublin, Ireland
[b]Insight Centre for Data Analytics, Dublin, Ireland
[c]School of Mechanical and Material Engineering, University College Dublin, Dublin, Ireland
*Correspondence should be addressed to D.M. (david.munoz@ucd.ie)

Neural control simulations are a powerful tool for evaluating principles of motor control that cannot be tested directly in conventional experimental settings. However, current controllers struggle with physiological grounding and are restricted to a small set of discrete behaviours, despite the inherent heterogeneity of human movement. Here, we propose a new neural controller, the Internal Model-based Modular Controller (IMMC), which can transition between multiple lower-limb motor tasks within a single simulation. The architecture comprises a simplified model of the Mesencephalic Locomotor Region (MLR), which sends control signals to activate internal models (IMs). These IMs organise functional muscle synergies into task-specific networks that generate coordinated and stereotyped activity across multiple muscles. The IMMC performs Stand-To-Walk, Stand-To-Backward-Walking, Walking-To-Stand, and Backward-Walk-To-Stand transitions, and modulates gait speed by adjusting a single control signal. Across all behaviours, the simulated kinematics, muscle activation patterns and ground reaction forces were generally consistent with experimental observations. These findings suggest that interactions between internal models and functional muscle synergies offer a plausible mechanism for producing heterogeneous motor behaviours, providing a conceptual basis for more flexible neuromuscular control architectures.

Introduction

Predictive neuromuscular models can address gaps in the knowledge of human motor control by testing hypotheses about its inherent neurophysiology (Hicks et al., 2015). Particularly, models that include explicit formulations of neural control architectures can mimic the role of sensorimotor control in the generation of movements. Current neural controllers present architectures which normally include reflexes (Geyer & Herr, 2010; Song & Geyer, 2015), central pattern generators (CPG) (Taga et al., 1991), or a combination of both (Di Russo et al., 2023; Dzeladini et al., 2014; Severini & Muñoz, 2025). These architectures often present challenges related to dimensionality and physiological plausibility.

Reflex-based controllers implement reflex loops (Geyer & Herr, 2010; Muñoz et al., 2022; Song & Geyer, 2012, 2015; van der Kruk & Geijtenbeek, 2023) to drive walking with remarkable similarity to experimental data. These controllers have shown that several principles of legged mechanics observed in gait (e.g., compliant leg behaviour, ankle push-off, hip unloading, swing, leg retraction) can emerge from linear reflexes (Geyer & Herr, 2010). This indicates that the dynamics of walking heavily rely on sensory feedback, which are cyclically triggered, and not only on a prevailing feedforward control such as CPG circuits.

Reflex-based controllers struggle with control dimensionality, defined as the number of parameters that must be tuned to map a motion (Russo et al., 2014), requiring a pre-defined set of parameters for each gait pattern (Song & Geyer, 2012, 2015). A recent reflex-based controller (Ramadan et al., 2022) addressed this issue by including an inverse model layer that switches control parameters depending on the context.

CPG-based controllers (Di Russo et al., 2023; Dzeladini et al., 2014; Ogihara & Yamazaki, 2001; Severini & Muñoz, 2025; Taga et al., 1991) incorporate these nominal structures as the primary element of control. CPGs are networks in the spinal cord that produce rhythmic locomotor activity even in absence of higher-level control or sensory inputs (Grillner et al., 1981; Rybak et al., 2006). CPGs are typically implemented following a half-centre organisation (Brown, 1914). This scheme describes a pair of antagonistic neurons (half-centres) coupled by mutual inhibitory disynaptic connections, forming a rhythmic unit. Gait models based on half-centre organisation can control motion rhythm using a few parameters, reducing control dimensionality (Taga et al., 1991; Matsuoka, 1985). However, unlike reflexes, which are well documented (Prochazka, 2010; Rossignol et al., 2006), CPGs are not completely understood in humans (Minassian et al., 2017).

CPG- and reflex-based controllers are also typically task-specific, as different motor behaviours require a combination of specialised controllers. For example, Van der Kruk & Geijtenbeek (2023) developed a reflex-based Sit-To-Walk model that integrated distinct sit-to-stand and gait controllers. This controller specificity, together with the high dimensionality of the control parameters, limits the flexibility of these neural controllers. We recently showed that a hybrid CPG-reflexes architecture can reproduce both walking and cycling, although through distinct optimisation of the controller parameters (Severini & Muñoz, 2025). Thus, current controllers are better suited to experimental setups where motor tasks are well isolated but cannot explain the inherent heterogeneity of human locomotion.

Modularity and hierarchical control can integrate low control dimensionality within a physiological framework (Giszter et al., 2010). Modules, or muscle synergies, are considered to be functional units of spinal interneurons that generate specific patterns of muscle activation (Bizzi et al., 2008; Caggiano et al., 2016; Dominici et al., 2011). Modularity also reflects biomechanical and control constraints, as producing stereotyped motor output requires coordinated activation across muscles (Ting et al., 2015). The combination of a limited number of synergies in a hierarchical architecture results in different motor behaviours (Bizzi et al., 2008; Bizzi & Cheung, 2013). This suggests that a few control signals can handle multiple motor outputs, reducing control dimensionality. Sartori et al. (2013) proved that synergies can synthesize walking in feedforward simulations. Still, the synergies were pre-defined and directly applied as muscle stimulations instead of being derived as naturally arising modules. Aoi et al. (2019) and Di Russo et al. (2023) integrated synergies with a CPG-based controller. In these models, the synergies were periodically triggered by the CPG as bursts of activity. Thus, rather than exhibiting the continuous oscillatory dynamics of the half-centre organisation, the synergies represented a discretised CPG that still lacked physiological consistency. We recently showed that a CPG structure based on the Unit Burst Generation model (Grillner, 1985), where CPGs drive flexor and extensor muscles at the different joints, results in synergistic patterns reflecting those observed experimentally, This suggests that the motor modules observed in gait derive from co-activation of simpler CPG-based units (Severini & Muñoz, 2025). However, while this model also employs reflexes, the CPG and reflex structures are fully distinct with no shared functionalities (Rybak et al., 2006).

Here, we propose the Internal Model-based Modular Controller (IMMC) as a novel architecture that integrates functional synergies, mapping to the principles of legged mechanics, in a hierarchical system

that can replicate multiple lower limb motions (Figure 1). The architecture aims to reduce the number of parameters to map motion, while offering a physiologically plausible representation of CPG behaviour. The IMMC is based on five assumptions: i) motion can be mapped to a correct arrangement of functional synergies located in the spinal cord (Bizzi & Cheung, 2013); ii) some functional synergies have a reflexive nature (Ivanenko et al., 2006); iii) a task-specific network is the result of applying a specific pattern of excitatory and inhibitory synapses, here referred to as an internal model (IM), to a set of functional synergies (Levine et al., 2014); iv) a hypothetical higher layer, corresponding to the mesencephalic locomotor region (MLR), selects IMs in parallel or sequentially to accomplish specific objectives (Le Ray et al., 2011); and v) standing, forward walking and backward walking tasks share synergies (Allen et al., 2020; Chvatal & Ting, 2013; Zych et al., 2021).

The structure of the IMMC consists of four layers organised hierarchically. From higher to lower, the layers are: 1) Control layer, 2) Planner layer, 3) Synergistic layer, and 4) Motoneuron layer (Figure 1(A)). Signal propagation across layers is regulated by sets of gains (α, θ, β, γ, and δ). The Control layer represents a simplified model of the MLR and provides control signals to the Planner layer. This layer consists of the internal models (IMs), each one representing a specific motor task. When activated by an MLR control signal, an IM selects and assembles a task-specific subset of functional synergies into a network. The IM regulates the amplitude and temporal scaling of the functional synergy burst through the α, θ gains. Although the functional synergies are triggered by sensory afferents, the IM also sets inter-synaptic connections to coordinate the activity of the network (Figure 1(B)).

The Synergistic layer comprises six distinct functional synergies (S), each contributing to a specific phase of locomotion: S1) Compliant-leg-behaviour resists gravity by extending the lower limbs; S2) Ankle push-off generates forward propulsion of the body; S3) Hip unloading reduces weight support on the stance leg and facilitates swing; S4) Swing propels the swing leg forward; S5) Leg retraction decelerates the swing and positions the leg for landing; S6) Transition is an ad hoc functional synergy that eases the transition between motor tasks: standing, walking, and backward walking.

The lowest level is the Motoneuron layer, where motor pools integrate the inputs from the functional synergies and sensory afferents before activating the MTUs (Figure 1(B)). Synergy inputs are weighted by β gains prior to motor pool activation, while sensory afferents are modulated by δ gains. The motor pools are organised into antagonist pairs at each joint and are mutually inhibited through γ gains.

The resultant architecture functions as a polymorphic controller in which a limited set of control signals reorganise the synergy network to drive a simple biomechanical model to execute different tasks within a single simulation. We examine this capability across several transition scenarios: i) Stand-To-Walk (STW); (ii) Walk-To-Stand (WTS); (iii) Stand-To-Backward Walking (STBW); (iv) Backward Walking-To-Stand (BWTS); (v) forward gait speed transitions. Across these modalities, we assess the simulated motor dynamics (i.e., kinematics, muscle activations patterns, and ground-reaction forces) in relation to human data. Through these evaluations, we validate functional synergy recombination as a plausible mechanism for motion heterogeneity, supporting the conceptual validity of the IMMC and its potential as a complementary alternative to current neural controllers.

121

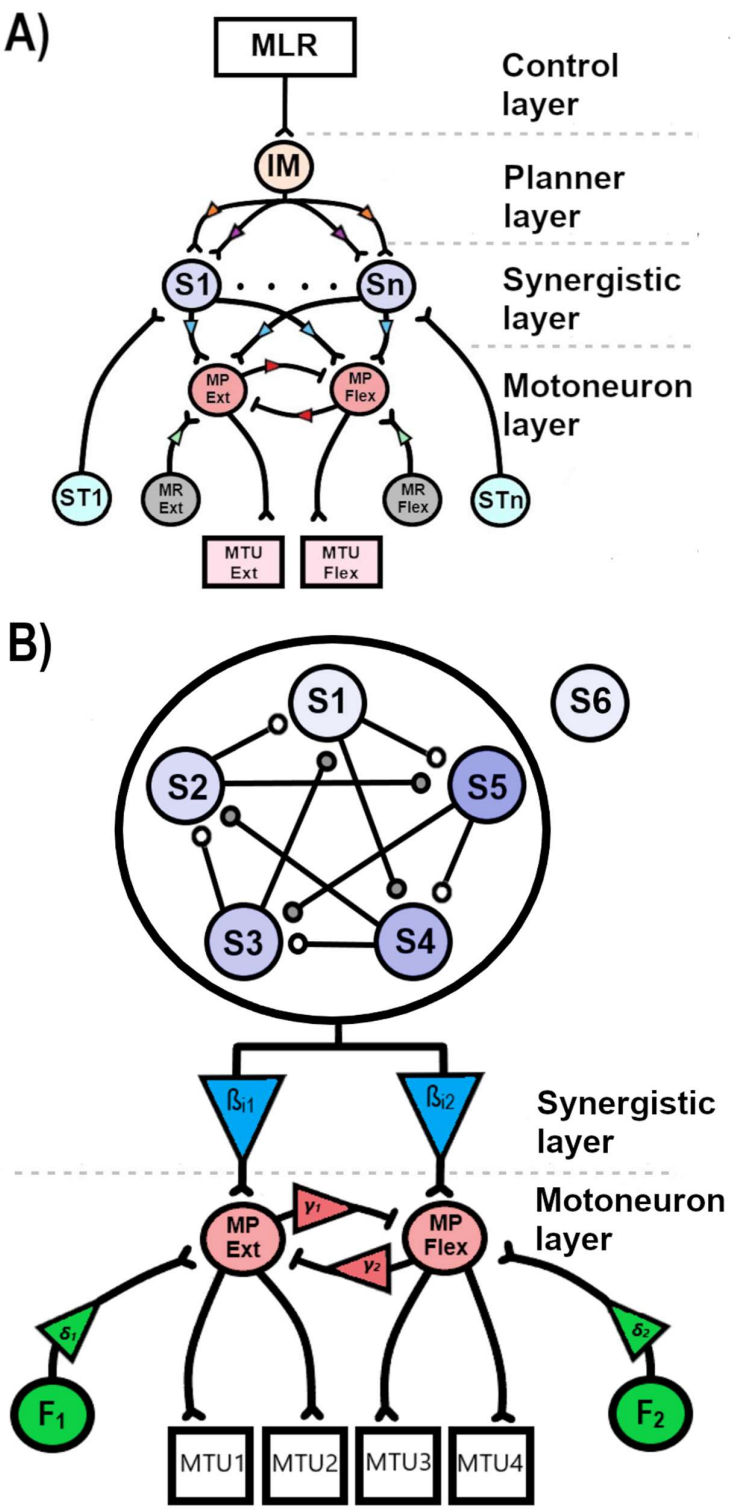

Figure 1. (A) Scheme of IMMC, showing the hierarchy, from top to bottom, of MLR, IMs, synergies, Motoneuron layer, and muscles. (B) Organisation of five synergies in a network and its connection to the motoneuron layer. The network shows two different inter-synaptic connections, phase coupling synapse (white circles) and inhibitory synapse (grey circles). Gains are indicated by triangles: α (orange), θ (purple), β (blue), γ (red), and δ (green). Acronym definitions. MLR: mesencephalic locomotor region, IM: Internal Model, S1: compliant-leg behaviour, S2: ankle push-off, S3: hip unloading, S4: swing, S5: leg retraction, S6: transition, $MP_{Ext/Flex}$: extensor/flexor motor pool, ST: sensory trigger, $MR_{Ext/Flex}$: extensor/flexor monosynaptic reflex, MTU: motor-tendon unit, F: sensory afferent.

Results

Gait transitions

We first evaluated the capacity of the IMMC to reproduce the transition behaviours targeted in this study: STW-WTS, STBW-BWTS, and forward-gait speed modulation (see Methods, *Task and speed transitions simulation protocol* section). Figure 2 illustrates these transitions by showing the evolution of the antero-posterior velocity of the torso Centre-of-Mass (CoM) across the full duration of the simulations: 15 s for the STW-WTS and STBW-BWTS tasks, and 10 s for the speed-transition trials (Videos for all the transitions are presented in the supplementary files: STW-WTS.mp4 STBW-BWTS.mp4, and forward_speeds.mp4).

The STW-WTS simulation (Figure 2(A), video STW-WTS.mp4) begins with the CoM in a static posture. The controller maintains a stable standing in the first half of the simulation, although slightly leaned backwards 5 ° to the normal vector to the ground (Figure 3). At $t_{STW\text{-}trans}$, set to 4.64 s, determined by the optimisation, the model breaks the standing posture by leaning the trunk forward. Stepping starts at t_{STW} = 5 s and the oscillation of the CoM stabilises at t_{steady} = 6.5 s. From t_{steady} to t = 10 s, the model maintains a stable gait, with an average walking speed is around 0.8 ms^{-1}. At $t_{WTS\text{-}trans}$ = 9.87 s, the CoM speed drops rapidly, and at t_{WTS} = 10s it begins to stabilise towards a quasi-static posture. This recovered standing is successfully maintained until the end of the simulation (t = 15 s). S

The IMMC model can achieve speed transitions by modulating $u_{o,gait}$, at t_{steady} (t = 6.5 s). The behaviour of the model until t_{steady} corresponds to the behaviour to the 1.3 ms^{-1} simulation. Figure 2(B) shows the instantaneous speed of CoM for the six speed transitions and the 1.3 ms^{-1} simulation. The respective average speeds are 0.8, 0.9, 1.2, 1.3, 1.5, 1.6, and 1.8 ms^{-1}. Video forward_speeds.mp4 show all forward gait simulations from 0.9 ms^{-1} to 1.8 ms^{-1}.

The STBW-BWTS simulation (Figure 2(C), video STBW-BWTS.mp4) presents the same standing dynamics as the forward condition until $t_{STBW\text{-}trans}$ = 4.21 s, when the model initiates a backward lean of torso. At t_{STBW} = 5 s, backward stepping begins, and the CoM speed oscillations before stabilising at approximately 0.8 ms^{-1} by t = 6 s. A steady backward walking is then maintained until $t_{BWTS\text{-}trans}$ = 9.77 s, when the model starts to decelerate. At t_{BWTS} = 10 s, the standing task is reinstated, and the CoM speed progressively stabilises toward zero, remaining in this quasi-static posture until the end of simulation at t = 15 s.

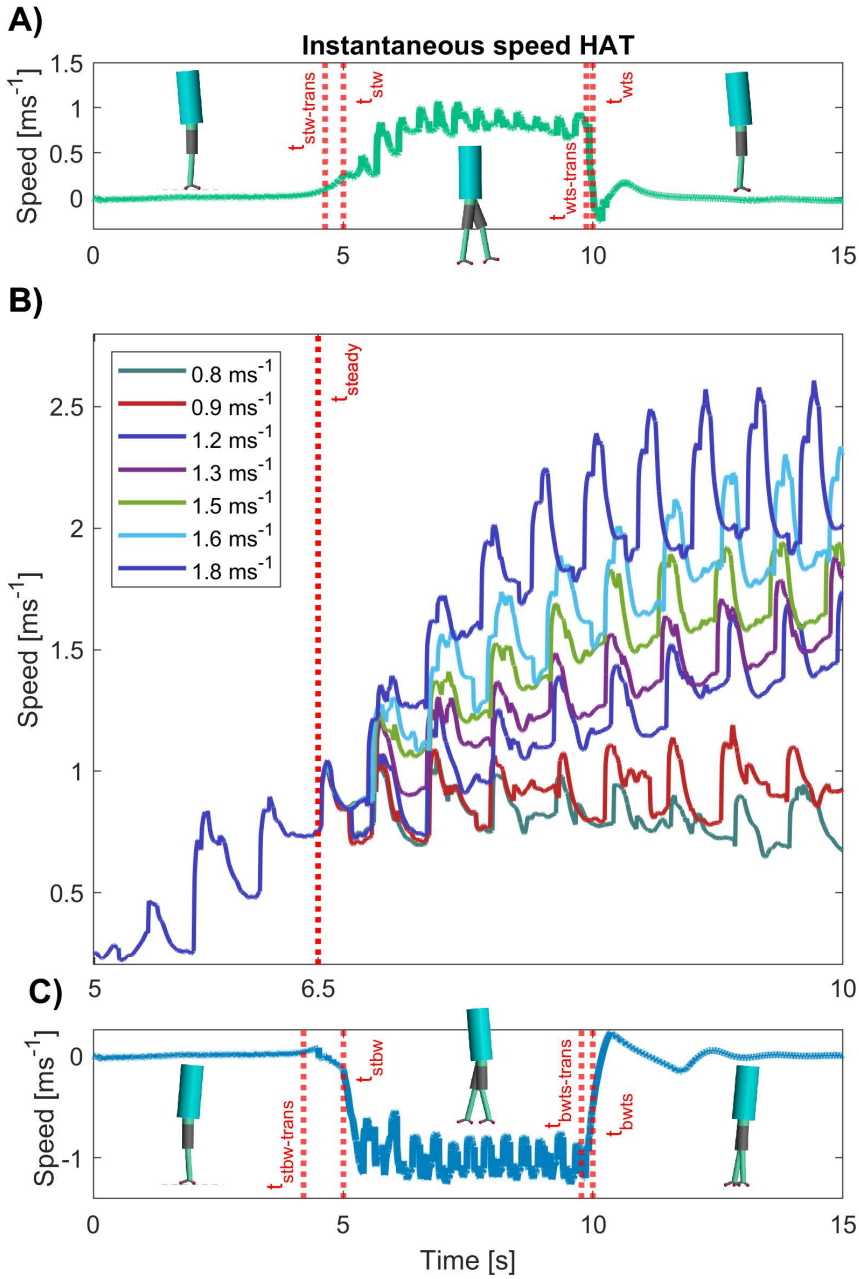

Figure 2. Instantaneous anterior/posterior speed of Head-Arms-Torso (HAT) for: (A) Stand-To-Walk (t = 5 s) and Walk-To-Stand (t = 10 s) transitions with a gait speed of 0.8 ms^{-1}. Transitions are started at $t_{STW\text{-}trans}$ = 4.64 s and $t_{WTS\text{-}trans}$ = 9.87 s, respectively. (B) Speed transitions for forward gait (from t_{steady} = 6.5 s) at 0.8, 0.9, 1.2, 1.3, 1.5, 1.6, and 1.8 ms^{-1}. (C) Stand-To-Walk (t = 5 s) and Walk-To-Stand with backward gait (t = 10 s). Transitions are started at $t_{STBW\text{-}trans}$ = 4.21 s and $t_{BWTS\text{-}trans}$ = 9.77 s, respectively.

151

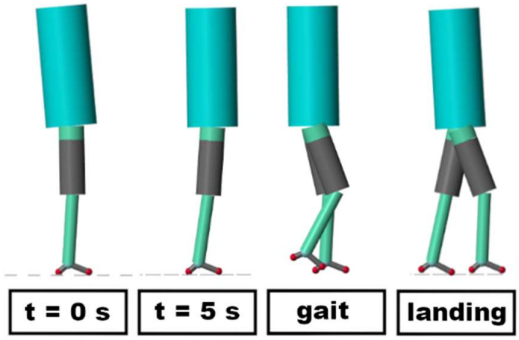

Figure 3. SWT transitions and first gait step.

Forward gait biomechanics

Figure 4(A) compares the simulated joint trajectories over the gait cycle with the angular positions in humans (Zych et al., 2021). The objective speed of this simulation is 1.3 ms^{-1}, the preferred by humans (Bastien et al., 2005; Kim & Kim, 2014). The simulation foot-off occurs at 66 % of the gait cycle, at the same instant than the experimental foot-off. The simulated hip, knee, and ankle angle are consistent with the experimental trajectories, showing high cross-correlation coefficients (r_{hip} = 0.82, Δ = 0 %; r_{knee} = 0.97, Δ = -2 %, r_{ankle} = 0.85, Δ = 0 %). Despite the strong correlations, hip exhibits more extension than its experimental counterpart at the beginning and end of the gait cycle. The simulated ankle is also slightly more dorsiflexed position at the beginning and end of the gait cycle. Figure 4(B) shows the GRFs. The results match the typical pattern of contact force during walking (Zych et al., 2021), with a good cross-correlation (r_{GRF} = 0.99, Δ = 0 %). The two peaks of the human GRF due to heel-strike and to ankle push-off are noticeable. However, the first peak is larger than in the experimental data, and the trace presents more instability, including a small bump before the second peak.

In Figure 4(C), the comparison of muscle activation patterns across the gait cycle is shown: hip flexors (HFL), gluteus (GLU), hamstrings (HAM), rectus femoris (RF), biceps femoris short head (BFSH), vastus (VAS), tibialis anterior (TA), soleus (SOL), and gastrocnemius (GAS). HAM was the only muscle which was not included in the experimental dataset. Overall, the simulated activation timing falls within the experimentally observed ranges reported by Zych et al. (2021). The cross-correlation coefficients are: r_{HFL} = 0.71, Δ = 13 %; r_{GLU} = 0.87, Δ = -2 %, r_{RF} = 0.63, Δ = -47 %; r_{BFSH} = 0.87, Δ = 0 %, r_{VAS} = 0.76, Δ = -19 %, r_{TA} = 0.69, Δ = -1 %; r_{SOL} = 0.94, Δ = 2 %, r_{GAS} = 0.65, Δ = 6 %.The muscles with the lowest similarity were RF, which did exhibit activation briefly during the first half of the gait cycle; TA, whose activity decreased prematurely at the beginning and the end of the cycle; and GAS, whose activation pattern was poorly corresponded with its experimental counterpart, except of the peak observed in the middle of the gait cycle. Video forward_speeds.mp4 (1.3 ms^{-1}) shows the complete 1.3 ms^{-1} simulation.

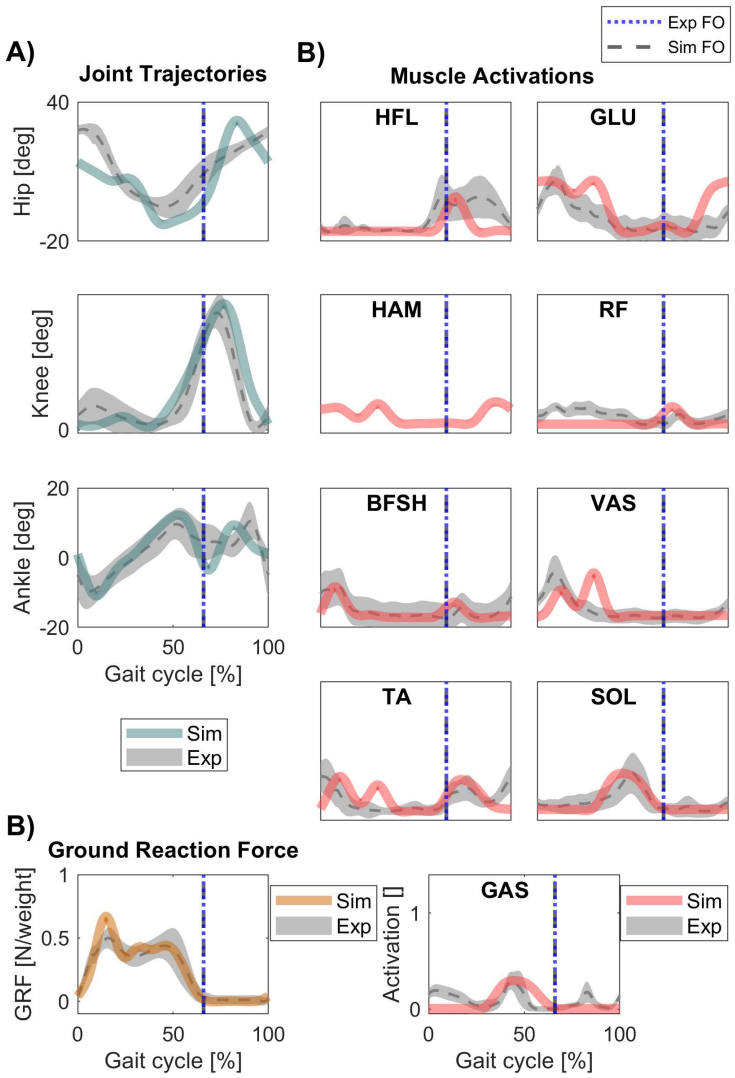

Figure 4. (A) Experimental and simulated angular positions for hips, knees, and ankles at 1.3 ms^{-1}. Green: simulated data, grey: experimental data. (B) GRF across the gait cycle at 1.3 ms^{-1}. Experimental and simulated GRF. Yellow: simulated data, grey: experimental data. (C) Muscle activation patterns along the gait cycle at 1.3 ms^{-1}. Orange: simulated data, grey: experimental data. Experimental data is given in the form of timing activation (HFL, GLU, HAM, SOL), or trajectories (RF, BFSH, VAS TA, GAS). Experimental angular positions, GRF, and muscle trajectories are given by Zych et al. (2021). Blue vertical dotted line: experimental foot-off (66 %), black vertical dotted line: simulation foot-off (66 %).

Speed transitions

The metabolic costs of transport are 5.40, 5.07, 4.20, 3.70, 3.73, 3.96, and 4.2 $Jkg^{-1}m^{-1}$ for the 0.8, 0.9, 1.2, 1.3, 1.5, 1.6, and 1.8 ms^{-1} speed simulations (Figure 5). For the speed of 1.3 ms^{-1}, the preferred walking speed by humans (Bastien et al., 2005; Kim & Kim, 2014), the average cost of transport is close to the physiological energy expenditure in humans (3.5 $Jkg^{-1}m^{-1}$) (Minetti et al., 2001; Umberger et al., 2003). The metabolic costs of transport at the central and faster speeds are consistent with experimental values (Bastien et al., 2005), although the costs at lower speeds are slightly higher in comparison.

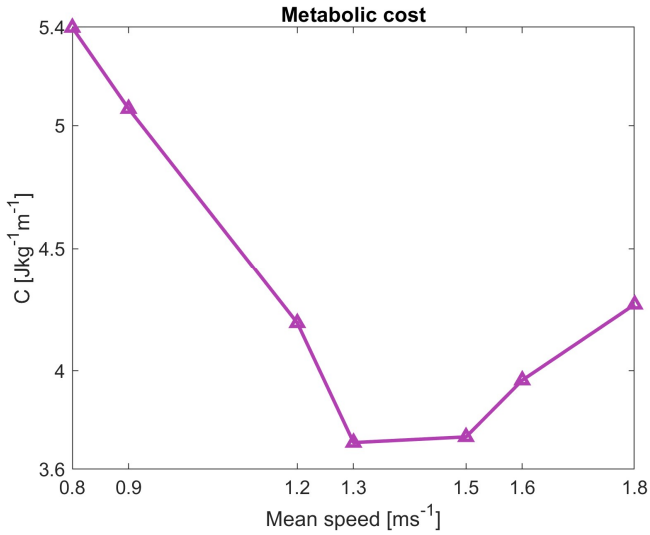

Figure 5. Metabolic cost of all the forward gait speeds.

The angular positions of the joints in the lower (0.8 ms^{-1}) and upper (1.8 ms^{-1}) transitions were compared to the experimental data of subjects walking at a slow and a fast speeds, respectively (Fukuchi et al., 2018) (Figure 6(A)). The cross-correlation coefficients (r) for hips and knees are 0.90 (Δ = 0 %) and 0.98 (Δ = -2 %) at slow speed, and 0.89 (Δ = 0 %) and 0.97 (Δ = -2 %) at fast speed. The ankle shows a cross-correlation below 0.7 at 0.8 ms^{-1} ($r_{ankle,0.8}$ = 0.64, Δ = -31 %), but above 0.7 at 1.8 ms^{-1} ($r_{ankle,1.8}$ = 0.78, Δ = -9 %). The ankle behaviour for both speeds is generally comparable with that observed for the 1.3 ms^{-1} simulations (Figure 4(A)). The joint trajectories of the rest of the simulations were also compared to the corresponding slow or fast speeds exhibited by subjects (Table 1). Except for the ankle angular position at 0.9 ms^{-1}, all the trajectories in the other speed simulations presented a good match (r > 0.7). The GRFs (Figure 6(B)) for the 0.8 ms^{-1} and 1.8 ms^{-1} speed simulations are similar to the experimental samples (Fukuchi et al., 2018), which is supported by the cross correlation analysis ($r_{GRF,0.8}$ = 0.93, Δ = -2 %; $r_{GRF,1.8}$ = 0.88, Δ = -2 %). The cross-correlation coefficients for the rest of speed transitions are above 0.7 (Table 1). Figure 6(C) shows the simulated muscle activation timing compared with experimental activity (Zajac et al., 2003). Also in this case, simulated patterns of activation are comparable to experimental ones, except for the RF, or the GLU and HAM for the 1.8 ms^{-1}, which show activity out of the shaded area. Video STW-WTS.mp4 shows the complete 0.8 ms^{-1} simulation and video forward_speeds.mp4 (1.8 ms^{-1}) shows the complete 1.8 ms^{-1} simulation.

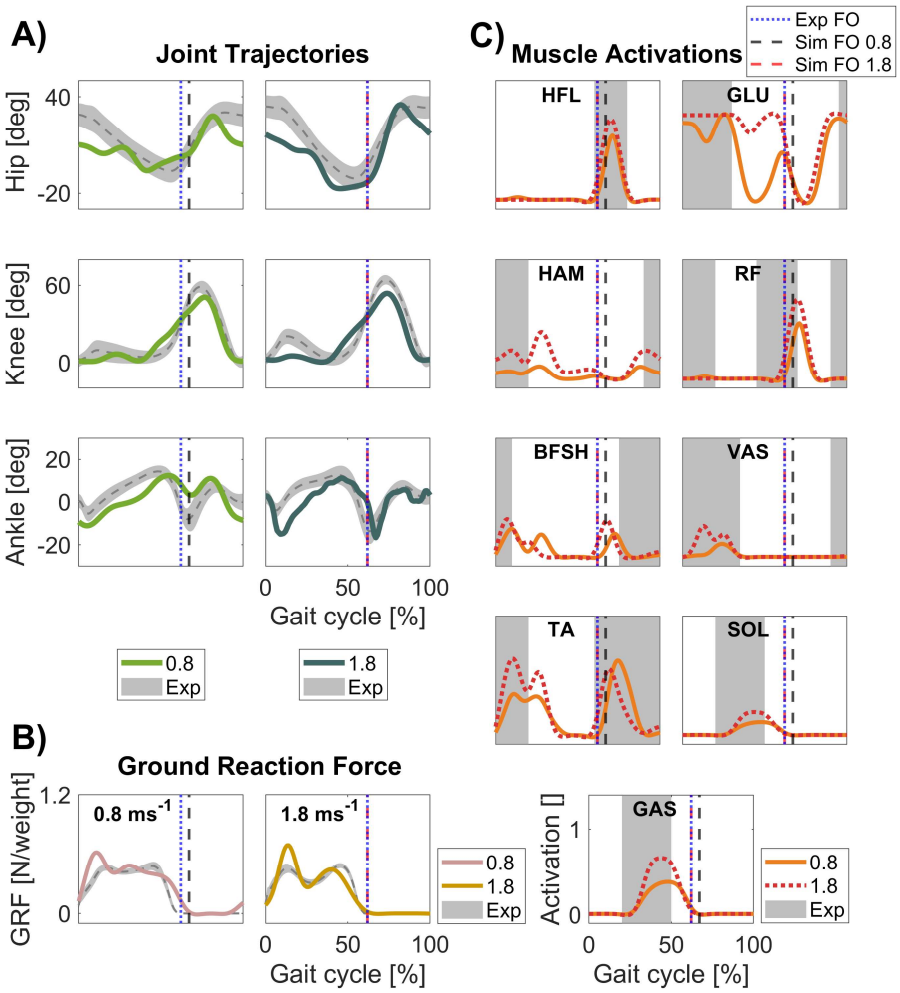

Figure 6. (A) Experimental and simulated angular positions for the lower (0.8 ms-1) and the upper (1.8 ms-1) transitions. Light green: simulated data at 0.8 ms-1, dark green: simulated data at 1.8 ms-1, grey: experimental data. (B) GRF for left foot along the duration of walking for the lower (0.8 ms-1) and the upper (1.8 ms-1) transition. Pink: simulated data at 0.8 ms-1, yellow: simulated data at 1.8 ms-1, grey: experimental data. (C) Muscle activation patterns for the left and right leg along the gait cycle for the lower and the upper transitions. Light orange solid line: simulated data at 0.8 ms-1, dark orange dotted line: simulated data at 1.8 ms-1, grey: experimental data. Experimental angular position and GRF are given by Fukuchi et al. (2018). Muscle activation timing is interpreted from Zajac et al. (2003). Blue vertical dotted line: generic experimental foot-off (62 %) indicated by Perry (2010), black vertical dotted line: simulation foot-off at 0.8 ms-1 (67 %), red vertical dotted line: simulation foot-off at 1.8 ms-1 (62 %).

202

Table 1. Cross-correlation coefficients and lags of the simulation and the experimental (Fukuchi et al., 2018) joint angular positions.

Speed [ms^{-1}]		r	lag [%]
0.8	Hip/Knee/Ankle/GRF	0.82/0.94/0.50/0.94	-1/1/5/0
0.9	Hip/Knee/Ankle/GRF	0.85/0.95/0.52/0.83	-1/3/5/4
1.2	Hip/Knee/Ankle/GRF	0.88/0.96/0.77/0.86	0/1/4/0
1.3	Hip/Knee/Ankle/GRF	0.90/0.95/0.67/0.87	0/1/6/4
1.5	Hip/Knee/Ankle/GRF	0.91/0.94/0.79/0.84	0/1/8/2
1.6	Hip/Knee/Ankle/GRF	0.91/0.94/0.85/0.85	0/0/7/0
1.8	Hip/Knee/Ankle/GRF	0.92/0.94/0.85/0.79	0/0/4/1

Backward gait biomechanics

Figure 7 (A) shows the comparison of the simulated trajectory of the joints over the backward gait cycle to the angular positions in humans (Zych et al., 2021). The simulation foot-off occurs at 68 % of the gait cycle, while the experimental foot-off occurs at 67 %. The simulated hip, knee, and ankle angles are consistent with the experimental trajectories, showing high cross-correlation coefficients (r_{hip} = 0.89, Δ = 0 %; r_{knee} = 0.92, Δ = 0 %, r_{ankle} = 0.86, Δ = -1 %). Although coefficients are high, hip is extended at the second half of the cycle, and the ankle is plantarflexed at the beginning and at the end of the cycle. Figure 7(B) shows the GRFs. The results match the typical pattern of contact force during walking (Zych et al., 2021), with a good cross-correlation (r_{GRF} = 0.96, Δ = 1 %). The two peaks of the human GRF due to heel-strike and to ankle push-off, are noticeable. However, these peaks and the valley between them are more noticeable than the experimental GRF.

In Figure 7(C), the comparison of muscle activation patterns across the backward gait cycle is shown, except for HAM. Overall, the simulated activation timing falls within the experimentally observed ranges reported by Zych et al (2021), with the clear exception of SOL and GAS which are not excited in the backward gait simulations. The cross-correlation coefficients for the rest of the muscles are: r_{HFL} = 0.86, Δ = 3 %; r_{GLU} = 0.90, Δ = 0 %, r_{RF} = 0.85, Δ = 0 %; r_{BFSH} = 0.93, Δ = 5 %, r_{VAS} = 0.96, Δ = 0 %, r_{TA} = 0.90, Δ = -11 %. Video STBW-BWTS.mp4 shows the complete STBW-BWTS simulation.

Discussion

Achievements of the IMMC

The IMMC achieved all target behaviours defined in the Introduction: i) Stand-To-Walk transitions; ii) Walk-To-Stand transitions; iii) Stand-To-Backward Walking transitions; iv) Backward Walk-To-Stand transitions; and v) forward gait speed transitions. These behaviours were obtained while operating under the four assumptions defined for its architecture.

Within this framework, the MLR selects the motors tasks by activating specific internal models. Each internal model then determines the set of functional synergies and its configuration, organising them within a task-specific network. Although this hierarchical architecture may appear complex, its operational workflow remains simple: the MLR requires only a small number of control signals to drive transitions between tasks. Similarly, forward speed modulation can be achieved through a single control signal. This combination of low control dimensionality, flexibility and reusability gives the IMMC

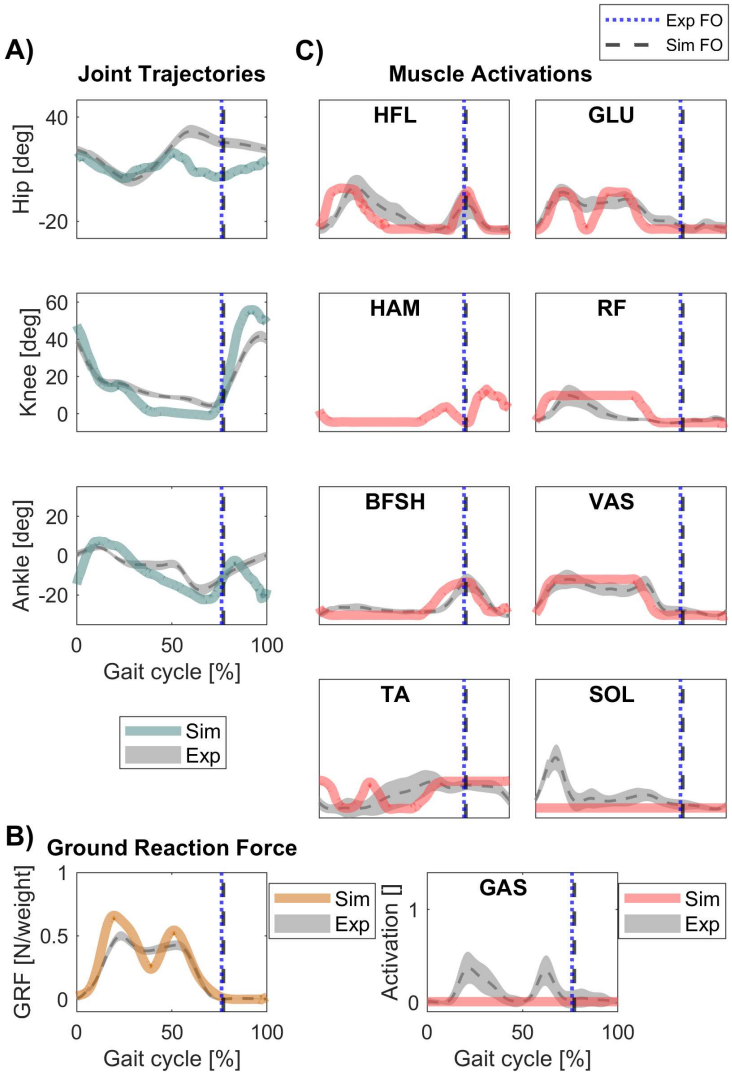

Figure 7. (A) Experimental and simulated angular positions for hips, knees, and ankles at backward gait simulations. Green: simulated data, grey: experimental data. (B) GRF across the gait cycle at backward gait simulations. Experimental and simulated GRF. Yellow: simulated data, grey: experimental data. (C) Muscle activation patterns along the gait cycle at backward gait simulations. Orange: simulated data, grey: experimental data. Experimental data is given in the form of timing activation. Experimental angular position, GRF, and muscle trajectories are given by Zych et al. (2012). Blue vertical dotted line: experimental foot-off (76 %), black vertical dotted line: simulation foot-off at backward gait simulations (77 %).

desirable properties for a neural controller and is consistent with experimental evidence (Allen et al., 2020; Chvatal & Ting, 2013; Ting et al., 2015; Zych et al., 2021).

The simulation results agree with most of the experimental biomechanics reported by Zych et al. (2021) and Fukuchi et al. (Fukuchi et al., 2018). The estimated metabolic cost of transport is close to physiological values. For the 1.3 ms^{-1} simulation, this value is around 3.7 $Jkg^{-1}m^{-1}$ compared to the 3.5 $Jkg^{-1}m^{-1}$ displayed by humans (Umberger et al., 2003) and other simulation controllers (Song & Geyer, 2012). For the speed transitions, the central speed, 1.3 ms^{-1}, presents the lowest metabolic cost.

Interestingly, this confirms the observation that humans prefer this pace for its metabolic efficiency (Bastien et al., 2005; Ralston, 1958; Minetti et al., 2001).

The simulated kinematics and muscular activation are generally consistent with experimental data. Foot-off events occurs at the 66 % of the gait cycle in both the simulated and the experimental forward walking and remains consistent across other experimental observations (Jacquelin Perry, 2010). The stance phase duration remains consistent across conditions (68 % in backward walking; 62 % in fast walking). Only in slow walking (0.8 ms^{-1}) simulated foot-off deviates from experimentally observed values.

Hip and knee angles follow experimental across most conditions. However, the hips show increased extension at the beginning and end of the gait cycle for the forward neutral (1.3 ms^{-1}), slow (0.8 ms^{-2}) and fast (1.8 ms^{-1}) walking simulations. In backward walking, hip extension appears only around the middle of the cycle. These deviations likely reflect the slight backward trunk lean during standing. Two factors may explain these irregularities in the hip angular position: (i) standing requires a synergistic structure that is more complex with respect to the one we implemented and in which the shared functional synergies play a more reactive role (Allen et al., 2020); and (ii) maintaining an upright torso requires a complementary control through torso-related vestibular reflexes (Angelaki & Cullen, 2008).

Ankle trajectories match experimental profiles but present the largest discrepancies in the cross-correlations. In the 0.8 ms^{-1} and 0.9 ms^{-1} simulations, the coefficients fall below 0.7. For both forward and the backward walking simulations the ankle deviates from the experimental pattern near the beginning and the end of the gait cycle. Such abnormalities are common in neural-controller simulation (Di Russo et al., 2023; Ramadan et al., 2022; Severini & Muñoz, 2025; Song & Geyer, 2015). However, other controllers (Geyer & Herr, 2010) (Dzeladini et al., 2014) show ankle kinematics that fit experimental data better than the IMMC. Schumacher et al. (2023) showed that abnormal trajectories for the ankle may depend on the selection of the musculoskeletal model. The musculoskeletal model used in this study is relatively simple, with the ankle implemented as a revolute joint and the foot represented by a rigid segment without additional musculature. Consequently, the foot is more susceptible to abrupt or jerky motions, and the ankle angle becomes more difficult to control.

This explanation is consistent with the dynamics observed in the GRFs and the activation patterns of the ankle related muscles. The GRFs show the characteristic two-peak waveform of walking gait, with the first peak related to heel strike and the second peak related to push-off. The fist peak is consistently higher than experimental data along all simulation conditions. The simplified rigidity of the ankle and foot may contribute to a slap-like motion immediately after the heel strike, when the forefoot drops to the ground. In addition, because the ankle sensory afferent relies on the distribution of reaction forces between the heel and toes, it tends trigger fast corrective motions. This likely produces the small bump observed before the second GRF peak in the forward walking simulations. A similar mechanism may occur during backward walking: the heel produces the slap motion after the forefoot strikes the ground, while the ankle sensory afferent drives adjustments than deepen the valley between two peaks as the system stabilises the ankle.

The muscle activation timings show good agreement between the simulation outputs and the experimental data for both forward and backward walking, as supported by the cross-correlation coefficients. The main exceptions are the rectus femoris, tibialis anterior, and gastrocnemius during the forward walking condition, and the soleus and gastrocnemius during backward walking. The rectus femoris behaves in a physiologically manner during backward walking but not during forward walking. One explanation is that forward and backward walking may not fully share functional synergies, as suggested by Zych et al (2021) or that the relationship between the different synergies is different for backward when compared to forward walking.

The discrepancies involving the ankle-related muscles, the tibialis anterior, soleus and gastrocnemius, are likely linked to the issues with the ankle mechanics described earlier. In fact, the drop in tibialis anterior activity at the beginning and end of the forward gait cycle corresponds to the excessive dorsiflexion observed at the same instants. For the soleus and gastrocnemius in backward walking, plantarflexor activity depends partly on concentric contractions produced by passive muscle elements, which are not represented in the current musculoskeletal model.

Novelty of the IMMC architecture

Our previous work on CPG- and reflex-based control (Severini & Muñoz, 2025) suggested that CPG-driven stimulation and sensory feedback act coordinated manner to generate walking rhythmogenesis. However, that framework did not explain how these mechanisms are intengraed into a nified control architecture, nor how their interactions are structured to support multiple motor behaviours. The IMMC addresses this gap by introducing the first polymorphic neural controller, as it allows objects of different types (e.g. functional synergies, reflexes, feedforward and feedback control) to be handled within a shared structural framework. This enables essential advantages respect to current controllers:

i) IMMC presents versatility to synthesise multiple motor behaviours with a unified architecture.

ii) In comparison to reflex-based controllers, IMMC presents hierarchical, low dimensional control.

iii) In comparison to CPG-reflex models, IMMC presents a physiological alternative to the half-centre organisation through functional muscle synergies.

iv) IMMC displays heterogeneous motor behaviours within a single simulation.

The IMMC does not require the combination of multiple controllers to achieve different tasks, like the Sit-To-Walk model of Van der Kruk & Geijtenbeek (2023), but rather the definition of task-specific IMs. The encapsulation of this information in IMs is flexible, as motion tasks can be changed while the rest of the control elements remain constant. For example, the motoneuron layer is shared across all motor tasks, and the reflex pathways remain constant, demonstrating the potential versatility of the IMMC. Moreover, instead of loading different parameter sets into the reflexes, the internal models rely on the reorganisation of the functional synergies across standing, forward walking, and backward walking. In this architecture, synergies function as shared functional motor blocks whose structural composition acquires task-specific meaning.

The low-dimensional control gives the IMMC another conceptual advantage over the reflex-based controllers (Geyer & Herr, 2010; Song & Geyer, 2012, 2015) which require the adjustment of the complete set of parameters for each gait pattern. Instead, the IMMC maps variations of a unique control signal to different speeds. Although optimisation of the IMMC was computationally demanding, all parameters belong to a unified architecture, and control dimensionality remains low.

The IMMC further contributes to ongoing discussions regarding the roles of synergies, reflexes, and feedforward mechanisms in locomotion. The design of reflex-based models often assumes that synergies and CPGs are impractical and difficult to validate (Geyer & Herr, 2010). In this view, motion would emerge from spinal reflexes which represent the principles of legged mechanics. Dzeladini et al. (2014) tried to reconcile both perspectives using CPGs as sensory predictors. Despite this effort, the controller presented limited capacity to replace the function of the reflexes. The IMMC integrates sensory afference with feedforward control: the expression of the functional synergies depends on the IMs but are triggered and modulated by sensory inputs. Furthermore, the functional synergies contribute to reduce muscular degrees of freedom (i.e., the number of muscle profiles that can achieve the same task), as multiple muscles are controlled by the same synergy. Future implementations with more MTUs can potentially benefit from this characteristic.

In comparison to CPG-based controllers, IMMC also offers a physiologically plausible alternative to feedforward control. Taga's models (1995a, 1995b, 1998; 1991) presented a CPG that could control speed by employing a unique signal. In those models, the architecture of the rhythm generator was based on the continuous oscillator of Matsuoka (1985). IMMC controls gait speed by tuning one control signal through the functional synergies, which are experimentally observable (Sartori et al., 2013; Ivanenko et al., 2004). Current controllers such those presented by Aoi et al. (2019) and Di Russo et al. (2023) also employed synergies. In those models, however, the synergies do not have physiological significance. They are a train of pulses triggered by a CPG. In the IMMC, the functional synergies represent the principles of legged mechanics which additionally incorporate the capacity of building different networks when are manipulated by the IMs.

Potential and limitation of the IMMC

The IMMC can be further developed to improve its dynamics and add new capabilities. A first step is to apply the controller to a more accurate musculoskeletal model, which would allow testing the use of the functional synergies to reduce the muscular degrees of freedom and for comparing different outputs of ankle trajectories. A more detailed characterisation of the functional synergies may enhance the capabilities of the IMMC. As in similar works (Di Russo et al., 2023; Severini & Muñoz, 2025), synergies were modelled as bell-shaped bursts, although more physiological activation profiles could be devised. The equation of the functional synergies can be substituted by another function that could reflect the dynamics of multiple sensory sources. Additionally, the role of some functional synergies may be revised. For example, the current implementation of the IMMC employs the *compliant-leg-behaviour* synergy to generate the baseline muscle activity to maintain standing (i.e., quiet standing). However, this synergy may be modified to reflect muscle responses involved in adjusting the upright posture in reactive standing and walking (Chvatal & Ting, 2013). If so, the controller could ideally still generalise this

functional synergy across both tasks in accordance with existing evidence (Allen et al., 2020). Improving the synergistic representation, combined with new IMs, could potentially allow the IMMC to achieve Walk-To-Run, Sit-To-Stand, and Sit-To-Walk transitions.

We also propose incorporating additional sensory receptors and monosynaptic reflexes in future work. The IMMC currently includes muscle force, and other proprioceptive inputs, which are enough for simulating standing and walking. These inputs are consistent with other models (Geyer & Herr, 2010; Muñoz et al., 2022). Still, gait rhythmogenesis depends on sensory afference (McCrea & Rybak, 2008). Thus, a more comprehensive set of muscular, cutaneous, vestibular. and other sensory sources (Rossignol et al., 2006), should be integrated into the IMMC. The implementation of these changes may allow the testing of the controller under different scenarios, including noisy sensory inputs to test the robustness of the architecture, or interactions across multiple surfaces. With these improvements, the IMMC could be used to investigate controller behaviour in realist settings. The MLR and the control signals represent the only supraspinal centre in the current IMMC, and its only source of volitional control. In humans, effective motion initiation is linked to tonic inputs from the MLR, which are modulated by other supraspinal centres (Le Ray et al., 2011). Despite this, higher structures, such as the cerebellum, motor, and premotor cortex were excluded from the IMMC. They introduce considerable complexity, and the model is focused on spinal control. Specifically, the motor adaptation provided by the cerebellum can update the IMs to replicate the split-belt treadmill (Choi & Bastian, 2007) or the robot-induced perturbation paradigms (Severini et al., 2020).

The IMMC adopts a node-based configuration, which is a convenient abstraction of neural populations and their synapses. This configuration is physiologically plausible but not anatomically accurate, and it aims to simplify the optimisation process. This may raise concerns in relation to motor pools, as they are modelled as linear systems. Actual motoneurons generate action potentials only when multiple inputs exceed a threshold, introducing nonlinearities into the system. However, if the nonlinear component of motoneuron output is considered as noise, the collective activity of the motor pools average out these variations, approximating the motor output as linear (Farina & Negro, 2015). Thus, our simplification of the motor pools does not necessarily contradict current neurophysiological studies.

The motor pools incorporate inhibitory disynapsis to coordinate antagonist dynamics but does not include a similar mechanism for right-left coordination. Although the trigger of the *hip unloading* synergy provides a biomechanical coupling between both legs ($Load_{ipsi}$ < 20 N), future versions of the IMMC should incorporate synaptic connections between left and right motor pools.

Overall conclusions

The IMMC provides a functioning multi-task neural controller capable of reproducing diverse lower-limb behaviours with low-dimensional control. Across all conditions, the simulated kinematics, muscle activations, and GRFs show general agreement with human data, validating the conceptual foundations of the IMMC. Its capacity to reorganise functional synergies, integrate sensory modulation, and transition across behaviours positions it as a promising complementary alternative to current neural controllers and a useful framework for investigating the mechanisms that underlie motion transitions.

Methods

Musculoskeletal model

The musculoskeletal model was implemented following the proportions detailed in Song and Geyer (2015). This configuration was chosen for its simplicity and suitability for testing an initial implementation of the IMMC. The model represents a human body of 1.80 m height and 80 kg weight. It has seven segments representing HAT (head-arms-torso), thighs, shanks, and feet. The model has 6 degrees of freedom (DoF) as revolute joints connecting the segments, hips, knees, and ankles (Figure 8). Three additional DoFs were added to define motion respect to the ground (longitudinal translation, anteroposterior translation, and pitch rotation). The muscle layer is composed of nine Hill-type muscolotendon units (MTUs): gluteus (GLU), hip flexors (HFL), hamstrings (HAM), rectus femoris (RF), vastus (VAS), biceps femoris short head (BFSH), gastrocnemius (GAS), soleus (SOL), and tibialis anterior (TA). Contact geometries consist of two spheres of 4 cm radius placed at the toes and heels of each foot (four in total). Sensory delays were added according to the position of the sensory source in the musculoskeletal model. Sources placed in a more distal position presents a longer delay as they are further from the spinal cord. They are short, medium, or long (5, 10, 20 ms_{-1}), according to their proximity to HAT/hips, knees, and ankles, respectively. The implementation follows Geyer's models (2010; 2012). These delays apply for all the sensory sources in the controller, including those related to trigger and modulate the functional synergies. The biomechanical model, the IMMC, optimisation and subsequent data analysis were implemented on Simulink/MATLAB R2022a.

IMMC architecture

The structure of the IMMC consists of four layers organised hierarchically. From higher to lower, the layers are: 1) Control layer, 2) Planner layer, 3) Synergistic layer, and 4) Motoneuron layer (Figure 1(A)). The Control layer represents a simplified model of the MLR. The planner layer represents the internal models. The Synergistic layer comprises six distinct functional synergies (S), each contributing to a specific phase of locomotion (Figure 9): S1) **Compliant-leg-behaviour** resists gravity by extending the lower limbs; S2) **Ankle push-off** generates forward propulsion of the body; S3) **Hip unloading** reduces

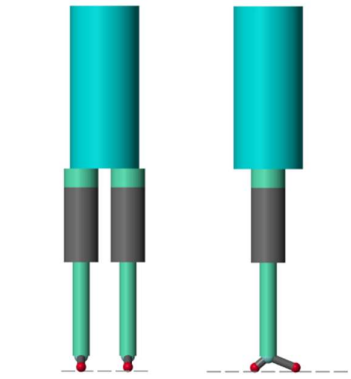

Figure 8. Right-side view of the musculoskeletal model during the standing (t = 0 s) and the walking (t = 5 s) behaviours.

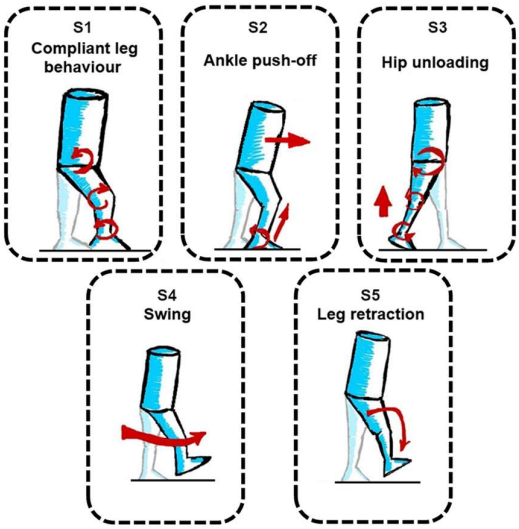

Figure 9. Principles of the legged mechanics. The figure presents the five principles of legged mechanics (Geyer and Herr, 2010) representative of the synergies implemented in the IMMC.

weight support on the stance leg and facilitates swing; S4) **Swing** propels the swing leg forward; S5) **Leg retraction** decelerates the swing and positions the leg for landing; S6) **Transition** is an ad hoc functional synergy that eases the transition between motor tasks: standing, walking, and backward walking.

The last layer is the Motoneuron layer where the various control signals are integrated and sent to the MTUs. The parameters regulating the activity of the layers of the IMMC were found through an optimisation process (see *Cost functions* section).

Control layer

The Control layer is the highest structure of the IMMC (Figure 1(A). It consists of the MLR, which controls movement initiation and IM control (Caggiano et al., 2016; Takakusaki, 2017). The MLR sends a limited number of control signals (u_o) to the IMs. Each control signal is specific to an internal model and activates it when set to any value other than zero. The stand control signal, $u_{o,stand}$, is defined as a discrete parameter that can take only two parameters: 0 (inactive) or 1 (active). In contrast, the gait and backward gait control signals, $u_{o,gait}$ and $u_{o,back}$, respectively, can assume multiple nonzero values regulating the rhythmogenesis of the functional synergies and the speed of gait. Specifically, forward gait-related u_o takes different values corresponding to different walking speeds (see *Task and speed transitions simulation protocol* section).

For transitions, four control signals operate on the transition internal model, activating Stand-To-Walk ($u_{o,STW}$), Walk-To-Stand ($u_{o,WTS}$), Stand-To-Backward Walking ($u_{o,STBW}$), and Backward Walking-To-Stand ($u_{o,BWTS}$) dynamics.

Planner layer

The Planner layer (Figure 1(A) contains the internal models (IMs), which regulate the relationship between the functional synergies. IMs presented here are a simplified version of the structures

proposed by Wolpert & Kawato (1998; 1998). Their role is to apply spatial and temporal constraints, expressed by α gains and θ gains, respectively, and regulate the inter-synaptic connections of a selected set of functional muscle synergies (Figure 1(B)). The α gains modulate the amplitude of the burst while burst speed is regulated by the θ gains. The inter-synaptic connections establish excitatory/inhibitory connections between functional synergies. The α gains, θ gains, and inter-synaptic connections ensure that the output of the synergy network matches the expected behaviour. Four IMs are included in the IMMC: one dedicated to stand (IM_{stand}), one for forward gait (IM_{gait}), one for backward gait, (IM_{back}) and one specialised in the transitions to and from stand, forward gait, and backward gait (IM_{trans}). The Planner layer defines which IM must be activated according to the Control layer. This action enables a specific network of functional synergies, blocking other possible forms of the controller. The IMs are side-specific, with independent copies for the left and right side. For speed control in forward gait, variations of $u_{o,gait}$ are used to map the i-th α and θ values of IM_{gait}, the $\alpha_{gait,i}$ and $\theta_{gait,i}$ gains, to new modified gains, $\alpha''_{gait,i}$ and $\theta''_{gait,i}$, establishing polynomial functions:

$$\alpha''_{gait,i} = \alpha_{gait,i} + \sum \alpha_{gait,n,i}\left(1 - u_{o,gait}\right)^n \quad (1)$$

$$\theta''_{gait,i} = \theta_{gait,i} + \sum \theta_{gait,n,i}\left(1 - u_{o,gait}\right)^n \quad (2)$$

where $\alpha_{gait,n,i}$ and $\theta_{gait,n,i}$ are the sets of modifying gains, n indicates the n-th order of the polynomial function, which was determined in the optimisation process. The control signal, $u_{o,gait}$, is equal to 1 for the basic speed of 1.3 ms^{-1}, the pace preferred by humans (Bastien et al., 2005; Kim & Kim, 2014). Slower and faster gaits are represented by lower and higher values of $u_{o,gait}$.

Synergistic layer

The six functional synergies are combined by the IMs to display standing, forward gait, backward gait, and the transition between these three behaviours. The first five functional synergies represent the principles of legged mechanics (Geyer & Herr, 2010). The sixth synergy is exclusively used in the transitions between standing and walking. Standing relies on one functional synergy (S1). In contrast, forward and backward walking preserve the same functional synergy set and structure, differing in the α and θ gains (Figure 10), and the position of the *ankle push-off* and *leg retraction* synergies

Although the activity of the functional synergies depends on the IMs, each of them has associated sensory triggers, which initiates the functional synergy, and sensory modulators, which modifies the synergy burst in real time (Table 2). Note that the sensory triggers and sensory modulator are subject to sensory delay (see *Musculoskeletal model* section), since they depend on sensory inputs. The six functional synergies are:

S1: Compliant-leg-behaviour. This functional synergy is shared by the IM_{stand} and IM_{gait}. In the IM_{stand}, the role of S1 is to keep the leg extended. In the IM_{gait}, it resists gravity during heel strike and allows double pendulum dynamics during stance. The sensory modulator of S1 is the positive force of the vastus muscle (F_{S1} = VAS F+), given the role of the knee extensors in compliant leg behaviour (Geyer & Herr, 2010). This modulator reflects the activity of the Golgi tendon organs which are deformed during

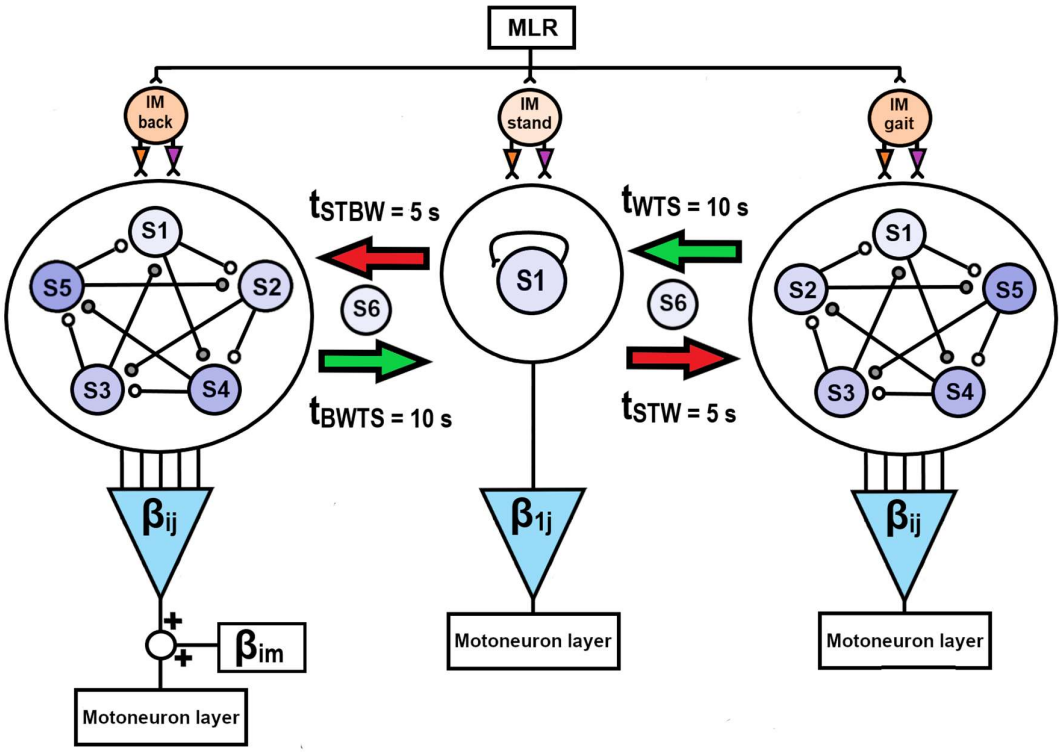

Figure 10. Flow of control of the IMMC from the MLR to the synergies. Three different networks are shown according to the controlling signal of the MLR, standing (middle), walking (right), and left (backward walking). Five different synergies are used to build these pathways. Note that β gains are constant for all scenarios. Backward walking incorporates corrective coefficients β_{im} into the β gains to account for the potential merging of the five forward-walking synergies with an additional set of m additional synergies that may be required for backward gait, as suggested by Zych et al. [45]. Walking and backward walking have the same synergy network but different α and θ gains. The sixth synergy accounts for all behaviour transitions as it incorporates multiple α gains, which are selected by the control signal. Gains are indicated by triangles: α (orange), θ (purple), and β (blue). Acronym definitions. MLR: Mesencephalic Locomotor Region, IM: internal model, S1: compliant-leg behaviour, S2: ankle push-off, S3: hip unloading, S4: swing, S5: leg retraction, S6: transition, β_{1j}: β gains from the first synergy to the j-th motor pool, β_{ij}: all the β gains.

muscle contraction, providing positive force feedback (Prochazka, 2010; Prochazka et al., 1997). As the functional synergy is activated during stance (Prochazka et al., 1997), its trigger is the foot-ground contact of the leg ($load_{ipsi}$ > 20 N). The delay is medium (10 ms) for the modulator and long (20 ms) for the trigger.

S2: Ankle push-off. This functional synergy provides forward impulse and the acceleration of the trailing leg (Zelik & Adamczyk, 2016). This is mechanically possible when the CoM reaches the leading leg ($CoM_x > heel_x$), which triggers the synergy. The positive force of the soleus muscle (F_{S2} = SOL F+) acts as the sensory modulator, since this muscle controls plantarflexion at late stance (Geyer & Herr, 2010). This functional synergy is only used in the IM_{gait} and IM_{back}. The delays for both the trigger and modulator are long-term (20 ms).

S3: Hip unloading. This functional synergy, which is active during late stance, assures that the stance leg unloads the weight of the body and prepares for swing. Hip flexion before swing correlates with extensor activity in the contralateral leg, implying that interlimb coordination must ensure the weight transfer to the leading leg (Dietz & Harkema, 2004). Then, the sensory trigger of this synergy is the load

on the contralateral leg ($load_{contra}$ > 20 N). No sensorial modulator is modelled for this synergy. This synergy is only in the IM_{gait} and IM_{back}. The delay is short-term (5 ms).

S4: Swing. The purpose of this functional synergy is to provide the forward impulse of the swing leg to complete a step. This functional synergy is triggered when the ipsilateral leg is free of the body weight ($Load_{ipsi}$ < 20 N) (Dietz & Harkema, 2004; Pang & Yang, 2000). No sensory modulator is modelled for this synergy. This functional synergy is only in the IM_{gait} and IM_{back}. The delay is long-term (20 ms).

S5: Leg retraction. This functional synergy consists of a leg extension that opposes the swing motion and facilitates the foot landing. Bhounsule & Zamani (2017) proposed that the swing-leg landing strategy depends on its kinematics during midstance. Considering midstance the instant when the gravity vector aligns with the leading leg, the synergy trigger is set to the heel of the swing leg passing over the CoM ($Heel_x$ > CoM_x). No sensory modulator is modelled for this synergy. This functional synergy is only used in the IM_{gait} and IM_{back}. The delay is long-term (20 ms).

S6: Transition. This is a functional synergy whose role is to ease the transition by breaking quiet standing before forward and backward gait initiation, or to slow motion and place feet together when transitioning back to stand. This functional synergy is not triggered by a sensorial event but by the activation of the corresponding control signals ($u_{o,STW}$, $u_{o,WTS}$, $u_{o,STBW}$, $u_{o,BWTS}$, > 0). This functional synergy has a sensory modulator (F_{trans}) which is based on the forward leaning of the HAT. The delay is short-term (5 ms). The synergy is only recruited by the IM_{trans}. The functions of the functional synergies are adapted for backward gait through the IM_{back} specific α and θ gains. In this condition, the sensory triggers associated with the *ankle push-off* synergy (S2) and the *leg-retraction* synergy (S5) are swapped, leading these two functional synergies to change position within the neural network (Figure 10). This reorganisation reflects the assumption of afferent reversal during backward locomotion(Duysens et al., 2004; Prochazka, 2010).

The IM_{trans} incorporates four sets of α and θ gains to adapt the *transition* synergy to STW, WTS, STBW and BWTS. The active control signal ($u_{o,STW}$, $u_{o,WTS}$, $u_{o,STBW}$, or $u_{o,BWTS}$) selects the appropriate set within the transition internal model.

Table 2. List of functional synergies and their corresponding function along the gait cycle, their corresponding sensorial triggers and modulators, and the associated gains.

Functional synergy	Function	Trigger	Modulator
1) Compliant leg behaviour	Resist gravitational pull / maintain quiet standing	Ipsilateral leg load > 20 N	Vastus positive force feedback
2) Ankle push-off	Forward impulse of the body	COM_x > $heel_x$	Soleus positive force feedback
3) Hip unloading	Weight transference	Contralateral leg load > 20 N	-
4) Swing	Forward impulse of the swing leg	Ipsilateral leg load < 20 N	-

5) Leg retraction	Swing leg landing	$Heel_x > COM_x$	-
6) Transition	Ease the Stand-To-Walk transition	$u_{o,STW}$, $u_{o,WTS}$, $u_{o,STBW}$, $u_{o,BWTS} > 0$	Θ_{HAT}

The six functional synergies (Figure 1(A)) operate independently until an IM organises them into a task-specific network. Each functional synergy also has a copy for each leg. The same synergy can be employed in different networks, pursuing diverse motor objectives. Modulations of one synergy can explain variations in the motor output, as observed in neurophysiological studies (d'Avella et al., 2003; Severini et al., 2020; Zych et al., 2021). A synergy is defined by a discrete bell-shaped burst of activity, as suggested by Ivanenko et al. (Ivanenko et al., 2006):

$$S_i = \alpha(1 + cos(2\pi\eta\omega(u_o > 0) + \pi)(t - \Delta t_{Si}) \tag{3}$$

where Si is the output of the i-th synergy, η is a sensory modulation of the burst, ω is a modulation generated by the next functional synergy, t is the simulation time, and Δt_{Si} accounts for any delay in the functional synergies. The parameter η is defined as:

$$\eta = \frac{\lambda_{Si}}{F_{Si} + \lambda_{Si}} \tag{4}$$

where λ_{Si} is a specific gain for the sensory afferent F_{Si} that modulates the i-th synergy. F_{Si} can be absent or different from the sensory afferent triggering the functional synergy. The function of the modulators is to prolong synergy activity when biomechanically necessary. If absent, then $F_{Si} = 0$, $\lambda_{Si} = 1$, $\eta = 1$.

The parameter ω is defined as:

$$\omega = \frac{\pi}{\theta_{i+1} - \theta_i} \tag{5}$$

where θ_i and θ_{i+1} are the θ gains for the current and the next functional synergy in the movement cycle, respectively. In the controller, each functional synergy is defined in a cycle that goes from 0 to 2π, irrespectively of whether it generates a rhythmogenesis or not. In the case where a single functional synergy is required for the organisation of a network like the standing behaviour and the transitions, θ_{i+1} is the θ gain of a virtual synergy that defines the frequency of the bursts. The θ gains specify temporal weights since they also determine the duration of each functional synergy in the total length of the walking cycle. The α gains represent spatial weighting, defining the partial contribution of a synergy to the system. The IMs also set within-synergy connections. IM_{stand} establishes an auto-excitatory synapse in the *compliant-leg-behaviour* synergy (S1) that generates a tonic control input. This self-sustained excitatory activity is derived from Rybak et al. (2006). In this simulation study, sustained activity from extensors and flexors are caused by rhythmogenesis deletions in the CPG. This dynamic can represent switches between tonic and rhythmic motor activity. For forward and backward walking, two inter-synaptic connections are established between functional synergies according to their relative positions (Figure 10). An inhibitory synapse is established from one synergy to the synergy two positions behind

($S_{i+2} \rightarrow S_i$). That means that $S_i = 0$ if $S_{i+2} > 0$. This mechanism avoids a functional synergy being still active when it is not needed anymore, and assures synchrony (Pfeuty et al., 2005). A second synapse is established as a phase coupling (Strogatz, 2000). Here, one functional synergy controls the rhythm of the previous synergy ($S_{i+1} \rightarrow S_i$). The phase coupling is defined as:

$$\Phi = -c \cdot sin(\phi_{i+1} + \phi_i + \pi) \tag{6}$$

where c is the strength of the coupling, manually tuned to 10, and φ_i and φ_{i+1} are the phases of two consecutive functional synergies. Equation (3) then becomes:

$$S_i = \alpha\big(1 + cos(2\pi\eta\omega(u_o > 0) + \pi + \Phi)\big)(t - \Delta t_{Si}) \tag{7}$$

An alternative formulation of equation (3) was devised for the first (*compliant-leg-behaviour*), the second (*ankle-push-off*), and the fifth (*leg-retraction*) synergies whose phase coupling was better explained by an amplitude factor:

$$S_i = \alpha(1 + cos(2\pi\eta\omega(u_o > 0) + \pi) - 10S_{i+1})(t - \Delta t_{Si}) \tag{8}$$

Motoneuron layer

The last layer is the Motoneuron layer (Figure 1(B)). The basic components of this layer are the motor pools. These are hypothetical well-defined groups of motoneurons that integrate outputs from different sources and send an activation signal to the MTUs (Maegele et al., 2002; Romanes, 1964). Here, motor pools are organised in agonist/antagonist pairs for each joint and are side-specific. Motor pools also integrate the output of monosynaptic reflexes. These reflexes maps to muscles acting on a specific joint through the corresponding motor pool, and do not stimulate muscles in synergy. In total, three linear functions are implemented, each specific to a joint. In the hip, joint-specific somatosensory inputs are proposed for hip joint control (Winter, 1995). Particularly, the controller uses hip angular position and angular velocity to stabilise the joint:

$$\kappa_{hip} = \left[\left(\phi_{hip} + \phi_{hip,o}\big(u_{o,gait} > 0\big)\right) \quad \dot{\phi}_{hip}\right] \begin{bmatrix} \delta_{q,ext} & \delta_{q,flex} \\ \delta_{\omega,ext} & \delta_{\omega,flex} \end{bmatrix} (t - \Delta t_{\phi}) \tag{9}$$

where κ_{hip} is the magnitude of the reflex input for the hip motor pools, φ_{hip} is the angular position of the hip, $\dot{\varphi}_{hip}$ is the angular velocity of the hip, $\delta_{q,ext}$ and $\delta_{q,flex}$ are the synaptic weights of the angular position for the hip extensor and the flexor motor pools, and $\delta_{\omega,ext}$ and $\delta_{\omega,flex}$ are the synaptic weights of the angular velocity to the hip extensor and the flexor motor pools, respectively. The parameter $\varphi_{hip,o}$ is the reference value for the hip joint in gait, only activated during the walk task ($u_{o,gait} > 0$). Δt_{φ} is the delay for φ_{hip} and $\dot{\varphi}_{hip}$, set to short (5 ms). Similarly, $u_{o,back}$ also activates a specific reference value for the hip during the backward gait task.

For the knee, the extensor motor pool is inhibited by 'pain', a nociception that measures the knee overextension (Geyer & Herr, 2010; Song & Geyer, 2015):

$$\kappa_{knee} = \delta_{knee} P_{knee}(t - \Delta t_P) \tag{10}$$

where δ_{knee} is the synaptic weight for pain of the knee, P_{knee}. Δt_P is the delay for P_{knee}, set to medium (10 ms). The afferent for the ankle motor pool, κ_{ankle}, is defined as the relative contact force on the toes and the heels of the feet:

$$\kappa_{ankle} = [\delta_{ankle,ext} \quad \delta_{ankle,flex}] \frac{f_{toe}}{f_{toe} + f_{heel}} (t - \Delta t_f) \tag{11}$$

where f_{ball} and f_{heel} are the contact forces for the toes and the heel with the ground, and $\delta_{ankle,ext}$ and $\delta_{ankle,flex}$ are the synaptic weights for the extensor and flexor motor pool, respectively. This reflex measures the CoP displacement that causes a reactive coactivation of the ankle muscles (Winter, 1995). Δt_f is the delay for f_{ball} and f_{heel}, set to long (20 ms). The activation output of the j-th motor pool is defined as:

$$y_j = \sum_{i=1}^{n} \beta_{ij} S_i + \sum_{k=1}^{m} \kappa_k - \gamma y' \tag{12}$$

where $ß_{ij}$ is the synaptic weight between the i-th synergy and the j-th motor pool, n is the number of motor pools in the system, and m is the number of monosynaptic reflexes connecting to that motor pool. Then, the motor pools act as a computational 'bottleneck' and the β gains constitute a second spatial filter for the functional synergies. The input y' is an inhibitory modulation from the antagonist motor pool, which synaptic weight is represented by the γ gains ($\gamma = \{\gamma_{hip}, \gamma_{knee}, \gamma_{ankle}\}$) (Figure 1). This interaction represents a typical agonist-antagonist disynaptic inhibition and is modified according to the forward and backward gait control signal:

$$\gamma' = \gamma + g\left(u_{o,gait/back} > 0\right) \tag{13}$$

where $g = \{g_{hip}, g_{knee}, g_{ankle}\}$ are specific constants that modify the γ gains, and γ' are the transformed γ gains. Each motor pool receives inputs from every functional synergy. As β_{ij} can take positive or negative values, this structure allows functional synergies to inhibit the activity of monosynaptic reflexes (Figure 11). The parameters γ and κ_k can be directly modulated by the IMs. The Motoneuron layer and its coupling with the functional synergies are presented in Figure 1(A), S_n being the n-th synergy and $MP_{Ext/Flex}$ being extensor/flexor motor pool. Muscles receive input from the motor pool to which they are anatomically related. The biarticular muscles gastrocnemius and hamstrings receive inputs from ankle extensor and hip extensor motor pools, respectively. To account for their dual contribution, the activation inputs are scaled by the factors S_{GAS} and S_{HAM}. The rectus femoris is fed by the hip flexor and knee extensor motor pools, with no scale factors.

The implementation of the β gains follows directly from the choice of functional synergies. Literature commonly identifies five synergies for forward gait (Ivanenko et al., 2004, 2006; Sartori et al., 2013). Zych et al. (2021) shown that backward walking can also be described using the same set of synergies as forward walking. However, this study did not discard that backward walking might require an additional, unspecified number m synergies. Ultimately, humans are less efficient at backward walking, requiring additional cognitive load. Thus, the five synergies for backward walking may be the merged

version of the five forward gait synergies and these *m* additional synergies. To represent this in the model, the *β* gains were adjusted through a corrective process:

$$\beta'_{ij} = \beta_{ij} + \beta_{im} \tag{14}$$

where β'_{ij} denotes the merged *β* gains for backward gait, and β_{im} are modifiers capturing the contribution of the potential m-th synergy. These corrected *β* gains replace the original ones in Equation 12, completing the workflow for backward walking (Figure 10).

The *transition* synergy (S6) is the only functional synergy associated with four distinct sets of *β* gains, with each set specifically assigned to the STW, WTS, STBW, and BWTS scenarios.

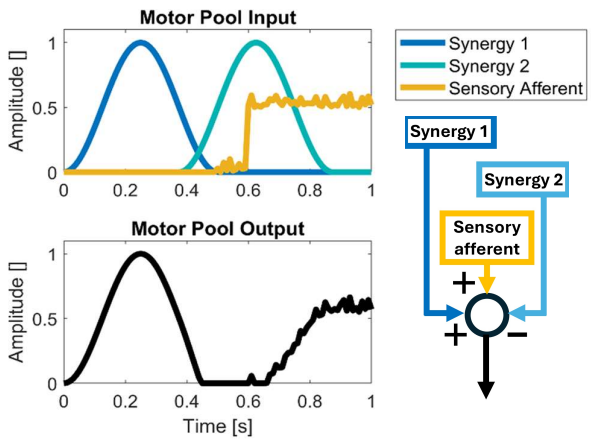

Figure 11. (Top) Hypothetical input to a motor pool, including two synergies and a sensory input. In this example, first synergy and sensory input have an excitatory synapse to the motor pool, while the second synergy has a negative synapse (Bottom) Resultant output of the motor pool. The sensory input is blocked by the second synergy.

Task and speed transition simulation protocol

The whole simulation is set to last a time (*t*) span of fifteen seconds. The first half of the simulation is dedicated to stand (0 s ≤ *t* < 5 s), the second is dedicated to gait (5 s ≤ *t* ≤ 10 s), and the third is dedicated to stand again (10 s ≤ *t* ≤ 15 s).

For the forward gait simulations, the time for the behaviour switch from stand to gait (*t* = 5 s) is denoted by t_{STW}, while the time to switch back to stand ((*t* = 10 s) is denoted by t_{wts}. The simulation workflow consists of the following steps:

1) At *t* = 0 s, the simulation initiates with the controller performing the standing task, displaying an upright, quasi-static posture. The MLR sets $u_{o,stand}$ to 1, and $u_{o,gait}$ to 0, causing the activation of IM_{stand} and the inactivation of IM_{gait}. IM_{stand} allows the recruitment of the *compliant-leg-behaviour* synergy, imposing $\alpha_{stand,1}$, $\theta_{stand,1}$, and $\theta_{stand,2}$ to the functional synergy. This configuration is identified as the stand network (Figure 10). The 5 s stand duration was set to demonstrate the capacity of IMMC to maintain a stable and functional upright posture before gait.

2) At an undetermined time ($t_{STW\text{-}trans}$) before t_{STW}, the IM_{trans} is activated, and the *transition* synergy is triggered to break the upright posture and lean the torso forward. The synergy has only one burst and it is not triggered again. The value of $t_{STW\text{-}trans}$ is determined during the optimisation (see *Walk-To-Stand and Backward-Walking-To-Stand optimisation* section). IM_{trans} presents a similar composition to IM_{stand} regarding the sets of α and θ gains, and the auto-excitatory synapse.

3) At t_{STW} = 5 s, the MLR switches $u_{o,stand}$ to 0 and $u_{o,gait}$ to 1. The synergy network reorganises from the standing to the forward walking configuration, recruiting all locomotor synergies and then initiating gait (right side of Figure 10). As IM_{gait} activates all the five functional synergies, except the transition one, it presents five α and five θ gains, and the two inter-synaptic connections. Each of them has their associated sensory triggers and modulators (Table I).

4) The speed increases to reach an average value of 1.3 ms^{-1}, the one preferred by humans (Bastien et al., 2005; Kim & Kim, 2014). Gait is maintained until t_{WTS} = 10 s.

5) Similarly to step 2, at the WTS transition time ($t_{WTS\text{-}trans}$), the IM_{trans} activates the *transition* synergy to stop motion and bring the feet together. When the MLR switches $u_{o,stand}$ back to 1 and $u_{o,gait}$ to 0 at t_{WTS} = 10 s, the IM_{stand} is reactivated again and takes control of the motion in a coordinated manner. At this point, the walking rhythmogenesis dissipates, and the model returns to the quasi-static posture of standing. To demonstrate that stable standing has been successfully re-established, the stand task is maintained until the end of the simulation (t = 15 s). The value of $t_{WTS\text{-}trans}$ is also determined during the optimisation (see *Optimisation algorithms* section).

For the speed transitions, the fifth step is different. Instead of switching back to the stand task, at t = 6.5 s, when the 1.3 ms^{-1} walk simulation reaches a stable gait (t_{steady}) the MLR adjusts $u_{o,gait}$ to one of these values: 1.6, 1.4, 1.2, 1, 0.8, 0.6, or 0.4. Consequently, the α and θ gains of IM_{gait} are modified according to equations (1) and (2), allowing the control of speed. The target speeds for the new values of $u_{o,gait}$ are 0.8, 0.9, 1.2, 1.3, 1.5, 1.6, and 1.8 ms^{-1}, respectively. The model maintains the new speed until the end of simulation at t = 10 s.

It is important to note that the STW-WTS uses the lowest walking speed (0.8 ms^{-1}). For this reason, the controller sets $u_{o,gait}$ = 1.6, instead of the default value of 1, at the third step of the protocol.

For backward gait, the STBW-BWTS workflow follows the same protocol than forward gait: 1) At t = 0 s, the MLR sets $u_{o,stand}$ = 1, and $u_{o,back}$ = 0, activating the standing task during the first five seconds of the simulation. 2) At the undetermined time $t_{STBW\text{-}trans} < t_{STBW}$ = 5 s, the IM_{trans} is activated, and the *transition* synergy is triggered to break the upright posture and initiate backward lean of the torso. The value of $t_{STBW\text{-}trans}$ is also determined during the optimisation (see *Optimisation algorithms* section). 3) At t_{STBW} = 5 s, the MLR switches $u_{o,stand}$ to 0 and $u_{o,back}$ to 1, initiating backward walking network. This configuration is similar to the forward walking one but swapping the positions of the *ankle push-off* and *leg retraction* synergies (left side of Figure 10). 4) The speed increases to an average value of 0.8 ms^{-1}, which is maintained until t_{BWTS} = 10 s. 5) At $t_{BWTS\text{-}trans}$, the IM_{trans} activates the *transition* synergy, and at t_{BWTS} the MLR switches $u_{o,stand}$ back to 1 and $u_{o,back}$ to 0, deactivating the backward walk task and

reinstating the stand task. The simulation then maintains standing until the end of simulation at t = 15 s.

Note that these simulation protocols, which are the main objective of this study, can be only obtained after optimising the controller. Given the complexity of the simulations, the motor tasks were optimised following a staged procedure. First, the standing and forward walking tasks, together with the STW transition, were optimised. These were followed by the optimisation of the forward walking speed transitions. The backward walking task and the STBW transition were then optimised. Finally, the WTS and BWTS transitions were optimised based on the outcomes of the corresponding earlier stages.

Optimisation algorithms

The optimisation algorithm is the Covariance Matrix Adaptation Evolution Strategy (CMA-ES) (Hansen, 2006). This algorithm is often used for neuromuscular simulations because the cost function is evaluated independently in each iteration, making it relatively resilient to the inherent noise of biomechanical systems (Zhang et al., 2017). Standing, transition, and forward walking behaviours require an optimisation process with three stages. In each stage, a specific set of parameters is optimised, with the IMMC having a total of 68 parameters. In the first stage, only the standing behaviour is optimised. Thus, stand is maintained along the simulation by setting the MLR to neither trigger the *transition* synergy nor switch to gait in the step 2 and 3 of the simulation protocol, respectively. Since stand is the only behaviour displayed in stage 1, only 19 parameters, related IM_{stand} and the Motoneuron layer, are adjusted. The parameters include the $ß$ gains related to the *compliant-leg-behaviour* synergy, $ß_{1j}$, the δ gains of equations (9-11), the three γ gains of the motor pools, the biarticular scale factors, and the λ gain associated with the first synergy, λ_{S1}. The θ and α gains of the IM_{stand} were hand-tuned to achieve a fast activation of the first synergy. This minimised the number of parameters to optimise and facilitates the convergence of the first stage. The $\alpha_{stand,1}$ gain was set to 0.5, and $\theta_{stand,1}$ and $\theta_{stand,2}$ were set to 0 and 0.25, respectively. A critical element of the cost function to minimise during this stage is the mass-specific energy consumption (E). Once E decreases below 2.5 Wkg^{-1} (i.e., twice the physiological consumption in humans (Umberger et al., 2003)) the optimisation proceeds to the stage 2. In stage 2, the MLR is set to trigger the at t = 5 s. As stand and gait are both optimised at this stage, all 68 parameters of the controller are optimised, including the 19 parameters already optimised in stage 1. The 49 parameters related to gait have previously been hand-tuned to initial values replicating three alternating steps (left-right-left). When the parameters are optimised to achieve gait for at least 3 seconds (8 s in total, including the 5 s for stand) and reduce E below 3 Wkg^{-1}, the optimisation progresses to stage 3. The requirement of E is higher than in stage 1 because the *transition* synergy increases the global stand metabolic cost. Stage 3 aims at optimising forward walk. Thus, only the 49 parameters of gait are optimised. These are the five $\alpha_{gait,i}$ gains and five $\theta_{gait,i}$ gains for the IM_{gait}, the STW dedicated gains of IM_{trans}, $\theta_{STW\text{-}trans,6}$ and $\theta_{STW\text{-}trans,1}$, the rest of the $ß$ gains of the system ($ß_{ij} \backslash ß_{1j}$), including the six $ß$ gains of the *transition* synergy for STW, $t_{STW\text{-}trans}$, λ_{S2}, λ_{S6}, the three g gains, and the reference angular position for hip ($\varphi_{hip,o}$) in equation 9. The gain $\alpha_{STW\text{-}trans,6}$ is set to 0.5. The 19 parameters related to stand are kept at the values found in stage 2. The third stage continues until the

end of the optimisation process, with a maximum of 600 iterations. The CMA-ES algorithm was set to 5 parents and 40 offspring in each generation. Equation (16) shows the flow of stages:

$$stage = \begin{cases} 1, \\ 2 \quad if stage = 1 \quad \& \quad E < 2.5, \\ 3 \quad if stage = 2 \quad \& \quad E < 3 \quad \& \quad t_{sim} > 8 \end{cases} \tag{15}$$

For the backward walking simulation, the stand task is represented by the same 19 parameters found in the stage 1 of the STW optimisation. Consequently, the model performs the same standing behaviour. The parameters to be optimised are those related to the STBW transition in the IM_{trans} ($\theta_{STBW\text{-}trans,6}$, $\theta_{STBW\text{-}trans,1}$, and $t_{STBW\text{-}trans}$), the six β gains of the *transition* synergy for STBW, the $ß_{im}$ gains of equation 14, the ten α and θ gains of IM_{back}, and the hip reference ($\varphi_{hip,o}$) of equation 9. In total, 49 parameters were optimised for backward walking. The gain $\alpha_{STBW\text{-trans},6}$ was fixed at 0.5.

The 49 parameters were initialised through manual tuning to reproduce a backward lean of the torso and replicating two alternating steps (right-left). The optimisation process was run for a maximum of 600 iterations, using the CMA-ES algorithm with 5 parents and 40 offspring per generation and a unique stage for backward walking.

The WTS and BWTS transitions are implemented as five-second extensions of the previously optimised STW (using the 0.8 ms^{-1} configuration, see *Speed transition optimisation* section) and STBW simulations, enabling the model to re-establish a stable standing posture after a forward or backward walking Each transition requires the optimisation of nine parameters, giving a total of 18 additional parameters. These include the two sets of six β gains for the *transition* synergy (one for WTS and one for BWTS), the IM_{trans} gains associated with both transitions ($\theta_{WTS\text{-}trans,6}$, $\theta_{WTS\text{-}trans,1}$, $\theta_{BWTS\text{-}trans,6}$, $\theta_{BWTS\text{-}trans,1}$), as well as $t_{WTS\text{-}trans}$ and $t_{BWTS\text{-}trans}$. The gains $\alpha_{WTS\text{-trans},6}$ and $\alpha_{BWTS\text{-trans},6}$ were fixed at 0.5. The simulation employs the same parameters for standing and forward/walking. Thus, only the WTS and BWTS are optimised in their respective processes. The optimisations run for a maximum of 300 iterations, using the CMA-ES algorithm with 8 parents and 16 offspring per generation.

The completed version of the IMMC counts with a total of 175 parameters.

Cost functions

For each task, the optimisation process used a dedicated cost function: standing (J_{stand}), forward walking (J_{gait})), backward walking (J_{back}), and transitions from forward/backward walking back to standing ($J_{WTS\text{-}BWTS}$).

The cost function employed during stand optimisation, J_{stand}, tries to maximise time without falling while minimising energy consumption (E):

$$J_{stand} = (t_{max} - t_{sim}) + E \tag{16}$$

where t_{max} is the maximum time of simulation (10 s), and t_{sim} is the time without falling. E (Wkg^{-1}) is defined according to Umberger et al. (2003) (see Supplementary Material). The cost function for forward gait (J_{gait}) is defined as:

$$J_{gait} = (t_{max} - t_{sim}) + 10|v_{tgt} - v_{sim}| + P + C \quad (17)$$

where t_{max} is set to 10 s, giving 5 s each for stand and gait, v_{tgt} is the objective speed of the simulation (at this stage, 1.3 ms^{-1}, representing the self-selected gait speed observed in humans), v_{sim} is the average speed achieved during the simulation, P is pain (the sum of joint torques when soft limits are exceeded) and C ($Jkg^{-1}m^{-1}$) is the metabolic cost of transport (Bastien et al., 2005; Ralston, 1958) (see Supplementary Material). Please note that speed objective of 1.3 ms^{-1} was prioritised. The STW-WTS protocol was achieved once obtaining the parameters for the 0.8 ms^{-1} simulation.

The cost function for backward gait (J_{back}) is defined as:

$$J_{back} = (t_{max} - t_{sim}) + 10|v_{tgt} - v_{sim}| + \frac{AP}{2} + C \quad (18)$$

where t_{max} =10 s, giving 5 s each for stand and backward gait, v_{tgt} is the target speed of the simulation (arbitrary chosen to be 0.8 ms^{-1}), and v_{sim} is the average simulated speed. AP is the deviation of the angular positions of the joints at heel strike respect to their mean. AP was included instead of P because backward walking normally converged to an irregular pace.

The cost function is identical for both transitions back to stand ($J_{WTS\text{-}BWTS}$) and is defined as:

$$J_{WTS-BWTS} = (t_{max} - t_{sim}) + 10|heel_{RX} - heel_{XL}| + E \quad (19)$$

where t_{max} = 15 s is the total simulation time and t_{sim} is the time completed without falling. The terms $heel_{XR}$ and $heel_{XL}$ represent the anteroposterior positions of the right and left heel and are used to evaluate the final distance between the feet in the recovered standing position.

Speed transition optimisation

The optimisation of the forward speed gaits follows a different process respect to the other tasks. The parameters found in the 1.3 ms^{-1} walk optimisation ($u_{o,gait}$ = 1) were used as set values for the speed optimisations. Six sets of modifiers, one common for all the α gains and five for the θ gains ($\alpha_{gait,m,1}$, $\theta_{gait,m,i}$ for i = 1-5) were added as follows:

$$\alpha'_{gait,i} = \alpha_{gait,i} + \alpha_{gait,m,1}(1 - u_{o,gait}) \quad (20)$$

$$\theta'_{gait,i} = \theta_{gait,i} + \theta_{gait,m,i}(1 - u_{o,gait}) \quad (21)$$

where $\alpha_{gait,i}$ and $\theta_{gait,i}$ are the i-th original gains, and $\alpha'_{gait,i}$ and $\theta'_{gait,i}$ are the resultant modified gains. The modifiers are optimised by the CMA-ES algorithm with 8 parents and 16 offsprings, while the number of iterations is 300. The cost function (J_{trans}) is defined as:

$$J_{trans} = 35|v_{tgt} - v_{sim,last}| + C + \frac{AP}{3} \quad (20)$$

where v_{tgt} is the target speed, $v_{sim,last}$ is the speed of the centre of mass in the anteroposterior axis in the last gait cycle to avoid excessive acceleration. As six sets of $\alpha_{gait,m,1}$ and $\theta_{gait,m,i}$ were calculated, a total of 36 gains were obtained. The aim is to find the modifiers $\alpha_{gait,n,i}$ and $\theta_{gait,n,i}$, from equations (1-2). Thus, instead of switching between the six sets of modifiers, a unique set of common set of ten

parameters can map the different values of $u_{o,gait}$ to the target speed. For that purpose, a second optimisation process was performed (J_{trans2}) where the differences between the outputs of equations (20–21), $\alpha'_{gait,i}$ and $\theta'_{gait,i}$, and equations 1 and 2, $\alpha''_{gait,i}$ and $\theta''_{gait,i}$ were minimised:

$$J_{trans2} = \left|\alpha'_{gait,i} - \alpha''_{gait,i}\right| + \left|\theta'_{gait,i} - \theta''_{gait,i}\right| \tag{23}$$

For the optimisation of J_{trans2} the algorithm used was the Sequential Quadratic Programming (SQP) algorithm, and the minimum was found using a numerical method that solves constrained nonlinear multivariable optimisation problems. This optimisation is iterated until J_{trans2} lowers below $1e^{-3}$. The new set of $\alpha_{gait,n,i}$ and $\theta_{gait,n,i}$ gains is composed of 40 gains, since the order of the equations (1-2) is set to four. This number is higher than the 36 $\alpha_{gait,m,1}$ and $\theta_{gait,m,i}$ gains, but adds the capability to modulate speed as a function of $u_{o,gait}$ without switching parameters. Please note that the 0.8 ms^{-1} simulation obtained through this process is used for the STW-WTS procedure instead of the 1.3 ms^{-1} configuration.

Evaluation & analysis

The results of the simulations using the optimised IMMC were evaluated based on the model's ability to complete the STW-WTS, STBW-BWTS, and forward speed transition protocols in response to changes in the controller form. These transitions rely on the polymorphic nature of the controller, achieved through the restructuring of the synergy network.

In addition, the simulation outputs were compared against experimental trajectories to assess the model's capacity to replicate gait patterns. Forward and backward gait, as well as the forward gait speed transition simulations, underwent the same evaluation procedure. The variables analysed included joint angular positions (hip, ankle, and ankle), ground reaction forces (GRFs), the muscle activation profiles over the gait cycle (0 - 100 %). For each condition, the results were averaged over the last three steps of each leg and time-normalised to 100 points, defining one gait cycle from heel-strike to heel-strike. GRFs were normalised to body weight.

Cross-correlation analysis was used to assess the similarity between experimental and simulated data, following common practice in predictive neuromuscular modelling (Geyer & Herr, 2010; Song & Geyer, 2015). The cross-correlation coefficients (r) and the corresponding lag (Δ)) were computed with 95% confidence bounds. We choose a simple threshold of $r \geq 0.7$ to indicate meaningful similarity.

For the forward and backward walking simulations, the outputs were compared against the experimental data from Zych et al. (2021). This dataset provided forward and backward walking trajectories for joint angles, ground reaction forces, and EMG profiles for all muscles except the hamstrings. EMG signals exhibit variability due to factors such as skin impedance and electrode placement (Hewson et al., 2003; Rainoldi et al., 2004), and some muscles, particularly deep muscles like the hip flexors, cannot be reliably measured with surface electrodes (Hu et al., 2011). Additionally, the simulated activations come from Hill-type muscle models, which do not represent EMG-derived activations in a physiologically faithful manner. For these reasons, the amplitudes of the simulated muscle activation profiles were scaled to match the maximum amplitude of their experimental counterpart.

Because Zych et al. (2021) did not provide data for different gait speeds, the forward speed transition simulations were compared against the dataset from Fukuchi et al. (2018), which reports joint angle trajectories and ground reaction forces for both small and fast walking speeds. However, this dataset does not include EMG measurements. Instead, muscle activation timing was referenced from the experimental profiles reported by Zajac et al. (2003).

Funding statement

This work was funded by Science Foundation Ireland (grants #21/FFP-P/10228 and #12/RC/2289_P2).

References

Allen, J. L., Carey, H. D., Ting, L. H., & Sawers, A. (2020). Generalization of motor module recruitment across standing reactive balance and walking is associated with beam walking performance in young adults. *Gait & Posture*, *82*, 242–247.

Angelaki, D. E., & Cullen, K. E. (2008). Vestibular system: The many facets of a multimodal sense. *Annu. Rev. Neurosci.*, *31*, 125–150.

Aoi, S., Ohashi, T., Bamba, R., Fujiki, S., Tamura, D., Funato, T., Senda, K., Ivanenko, Y., & Tsuchiya, K. (2019). Neuromusculoskeletal model that walks and runs across a speed range with a few motor control parameter changes based on the muscle synergy hypothesis. *Scientific Reports*, *9*(1), 369.

Bastien, G. J., Willems, P. A., Schepens, B., & Heglund, N. C. (2005). Effect of load and speed on the energetic cost of human walking. *European Journal of Applied Physiology*, *94*, 76–83.

Bhounsule, P. A., & Zamani, A. (2017). Stable bipedal walking with a swing-leg protraction strategy. *Journal of Biomechanics*, *51*, 123–127.

Bizzi, E., & Cheung, V. C. (2013). The neural origin of muscle synergies. *Frontiers in Computational Neuroscience*, *7*, 51.

Bizzi, E., Cheung, V. C., d'Avella, A., Saltiel, P., & Tresch, M. (2008). Combining modules for movement. *Brain Research Reviews*, *57*(1), 125–133.

Brown, T. G. (1914). On the nature of the fundamental activity of the nervous centres; together with an analysis of the conditioning of rhythmic activity in progression, and a theory of the evolution of function in the nervous system. *The Journal of Physiology*, *48*(1), 18.

Caggiano, V., Cheung, V. C., & Bizzi, E. (2016). An optogenetic demonstration of motor modularity in the mammalian spinal cord. *Scientific Reports*, *6*(1), 35185.

Choi, J. T., & Bastian, A. J. (2007). Adaptation reveals independent control networks for human walking. *Nature Neuroscience*, *10*(8), 1055–1062.

Chvatal, S. A., & Ting, L. H. (2013). Common muscle synergies for balance and walking. *Frontiers in Computational Neuroscience*, *7*, 48.

d'Avella, A., Saltiel, P., & Bizzi, E. (2003). Combinations of muscle synergies in the construction of a natural motor behavior. *Nature Neuroscience*, *6*(3), 300–308.

Di Russo, A., Stanev, D., Sabnis, A., Danner, S. M., Ausborn, J., Armand, S., & Ijspeert, A. (2023). Investigating the roles of reflexes and central pattern generators in the control and modulation of human locomotion using a physiologically plausible neuromechanical model. *bioRxiv*, 2023–01.

Dietz, V., & Harkema, S. J. (2004). Locomotor activity in spinal cord-injured persons. *Journal of Applied Physiology*, *96*(5), 1954–1960.

Dominici, N., Ivanenko, Y. P., Cappellini, G., d'Avella, A., Mondì, V., Cicchese, M., Fabiano, A., Silei, T., Di Paolo, A., & Giannini, C. (2011). Locomotor primitives in newborn babies and their development. *Science*, *334*(6058), 997–999.

Duysens, J., Bastiaanse, C., Smits-Engelsman, B. C., & Dietz, V. (2004). Gait acts as a gate for reflexes from the foot. *Canadian Journal of Physiology and Pharmacology*, *82*(8–9), 715–722.

Dzeladini, F., Van Den Kieboom, J., & Ijspeert, A. (2014). The contribution of a central pattern generator in a reflex-based neuromuscular model. *Frontiers in Human Neuroscience*, *8*, 371.

Farina, D., & Negro, F. (2015). Common synaptic input to motor neurons, motor unit synchronization, and force control. *Exercise and Sport Sciences Reviews*, *43*(1), 23–33.

Fukuchi, C. A., Fukuchi, R. K., & Duarte, M. (2018). A public dataset of overground and treadmill walking kinematics and kinetics in healthy individuals. *PeerJ*, *6*, e4640.

Geyer, H., & Herr, H. (2010). A muscle-reflex model that encodes principles of legged mechanics produces human walking dynamics and muscle activities. *IEEE Transactions on Neural Systems and Rehabilitation Engineering*, *18*(3), 263–273.

Giszter, S. F., Hart, C. B., & Silfies, S. P. (2010). Spinal cord modularity: Evolution, development, and optimization and the possible relevance to low back pain in man. *Experimental Brain Research*, *200*, 283–306.

Grillner, S. (1985). Neurobiological bases of rhythmic motor acts in vertebrates. *Science*, *228*(4696), 143–149.

Grillner, S., McClellan, A., & Perret, C. (1981). Entrainment of the spinal pattern generators for swimming by mechano-sensitive elements in the lamprey spinal cord in vitro. *Brain Research*, *217*(2), 380–386.

Hansen, N. (2006). The CMA evolution strategy: A comparing review. *Towards a New Evolutionary Computation: Advances in the Estimation of Distribution Algorithms*, 75–102.

Hewson, D. J., Hogrel, J.-Y., Langeron, Y., & Duchêne, J. (2003). Evolution in impedance at the electrode-skin interface of two types of surface EMG electrodes during long-term recordings. *Journal of Electromyography and Kinesiology*, *13*(3), 273–279.

Hicks, J. L., Uchida, T. K., Seth, A., Rajagopal, A., & Delp, S. L. (2015). Is my model good enough? Best practices for verification and validation of musculoskeletal models and simulations of movement. *Journal of Biomechanical Engineering*, *137*(2), 020905.

Hu, H., Meijer, O. G., van Dieën, J. H., Hodges, P. W., Bruijn, S. M., Strijers, R. L., Nanayakkara, P. W., Van Royen, B. J., Wu, W. H., & Xia, C. (2011). Is the psoas a hip flexor in the active straight leg raise? *European Spine Journal*, *20*, 759–765.

Ivanenko, Y. P., Poppele, R. E., & Lacquaniti, F. (2004). Five basic muscle activation patterns account for muscle activity during human locomotion. *The Journal of Physiology*, *556*(1), 267–282.

Ivanenko, Y. P., Poppele, R. E., & Lacquaniti, F. (2006). Motor control programs and walking. *The Neuroscientist*, *12*(4), 339–348.

Jacquelin Perry, M. (2010). Gait analysis: Normal and pathological function. *New Jersey: SLACK*.

Kim, W. S., & Kim, E. Y. (2014). Comparing self-selected speed walking of the elderly with self-selected slow, moderate, and fast speed walking of young adults. *Annals of Rehabilitation Medicine*, *38*(1), 101–108.

Le Ray, D., Juvin, L., Ryczko, D., & Dubuc, R. (2011). Supraspinal control of locomotion: The mesencephalic locomotor region. *Progress in Brain Research*, *188*, 51–70.

Levine, A. J., Hinckley, C. A., Hilde, K. L., Driscoll, S. P., Poon, T. H., Montgomery, J. M., & Pfaff, S. L. (2014). Identification of a cellular node for motor control pathways. *Nature Neuroscience*, *17*(4), 586–593.

Maegele, M., Müller, S., Wernig, A., Edgerton, V. R., & Harkema, S. (2002). Recruitment of spinal motor pools during voluntary movements versus stepping after human spinal cord injury. *Journal of Neurotrauma*, *19*(10), 1217–1229.

Matsuoka, K. (1985). Sustained oscillations generated by mutually inhibiting neurons with adaptation. *Biological Cybernetics*, *52*(6), 367–376.

McCrea, D. A., & Rybak, I. A. (2008). Organization of mammalian locomotor rhythm and pattern generation. *Brain Research Reviews*, *57*(1), 134–146.

Minassian, K., Hofstoetter, U. S., Dzeladini, F., Guertin, P. A., & Ijspeert, A. (2017). The human central pattern generator for locomotion: Does it exist and contribute to walking? *The Neuroscientist*, *23*(6), 649–663.

Minetti, A. E., Pinkerton, J., & Zamparo, P. (2001). From bipedalism to bicyclism: Evolution in energetics and biomechanics of historic bicycles. *Proceedings of the Royal Society of London. Series B: Biological Sciences*, *268*(1474), 1351–1360.

Muñoz, D., De Marchis, C., Gizzi, L., & Severini, G. (2022). Predictive simulation of sit-to-stand based on reflexive-controllers. *Plos One*, *17*(12), e0279300.

Ogihara, N., & Yamazaki, N. (2001). Generation of human bipedal locomotion by a bio-mimetic neuro-musculo-skeletal model. *Biological Cybernetics*, *84*(1), 1–11.

Pang, M. Y., & Yang, J. F. (2000). The initiation of the swing phase in human infant stepping: Importance of hip position and leg loading. *The Journal of Physiology*, *528*(2), 389–404.

Pfeuty, B., Mato, G., Golomb, D., & Hansel, D. (2005). The combined effects of inhibitory and electrical synapses in synchrony. *Neural Computation*, *17*(3), 633–670.

Prochazka, A. (2010). Proprioceptive feedback and movement regulation. *Comprehensive Physiology*, 89–127.

Prochazka, A., Gillard, D., & Bennett, D. J. (1997). Positive force feedback control of muscles. *Journal of Neurophysiology*, *77*(6), 3226–3236.

Rainoldi, A., Melchiorri, G., & Caruso, I. (2004). A method for positioning electrodes during surface EMG recordings in lower limb muscles. *Journal of Neuroscience Methods*, *134*(1), 37–43.

Ralston, H. J. (1958). Energy-speed relation and optimal speed during level walking. *Internationale Zeitschrift Für Angewandte Physiologie Einschliesslich Arbeitsphysiologie*, *17*(4), 277–283.

Ramadan, R., Meischein, F., & Reimann, H. (2022). High-level motor planning allows flexible walking at different gait patterns in a neuromechanical model. *Frontiers in Bioengineering and Biotechnology*, *10*, 959357.

Romanes, G. (1964). The motor pools of the spinal cord. *Progress in Brain Research*, *11*, 93–119.

Rossignol, S., Dubuc, R., & Gossard, J.-P. (2006). Dynamic sensorimotor interactions in locomotion. *Physiological Reviews*, *86*(1), 89–154.

Russo, M., D'Andola, M., Portone, A., Lacquaniti, F., & d'Avella, A. (2014). Dimensionality of joint torques and muscle patterns for reaching. *Frontiers in Computational Neuroscience*, *8*, 24.

Rybak, I. A., Stecina, K., Shevtsova, N. A., & McCrea, D. A. (2006). Modelling spinal circuitry involved in locomotor pattern generation: Insights from the effects of afferent stimulation. *The Journal of Physiology*, *577*(2), 641–658.

Sartori, M., Gizzi, L., Lloyd, D. G., & Farina, D. (2013). A musculoskeletal model of human locomotion driven by a low dimensional set of impulsive excitation primitives. *Frontiers in Computational Neuroscience*, *7*, 79.

Schumacher, P., Geijtenbeek, T., Caggiano, V., Kumar, V., Schmitt, S., Martius, G., & Haeufle, D. F. (2023). Natural and robust walking using reinforcement learning without demonstrations in high-dimensional musculoskeletal models. *arXiv Preprint arXiv:2309.02976*.

Severini, G., Koenig, A., Adans-Dester, C., Cajigas, I., Cheung, V. C., & Bonato, P. (2020). Robot-driven locomotor perturbations reveal synergy-mediated, context-dependent feedforward and feedback mechanisms of adaptation. *Scientific Reports*, *10*(1), 5104.

Severini, G., & Muñoz, D. (2025). A physiologically inspired hybrid CPG/Reflex controller for cycling simulations that generalizes to walking. *PLOS Computational Biology*, *21*(9), e1013494.

Song, S., & Geyer, H. (2012). *Regulating speed and generating large speed transitions in a neuromuscular human walking model*. 511–516.

Song, S., & Geyer, H. (2015). A neural circuitry that emphasizes spinal feedback generates diverse behaviours of human locomotion. *The Journal of Physiology*, *593*(16), 3493–3511.

Strogatz, S. H. (2000). From Kuramoto to Crawford: Exploring the onset of synchronization in populations of coupled oscillators. *Physica D: Nonlinear Phenomena*, *143*(1–4), 1–20.

Taga, G. (1995a). A model of the neuro-musculo-skeletal system for human locomotion: I. Emergence of basic gait. *Biological Cybernetics*, *73*(2), 97–111.

Taga, G. (1995b). A model of the neuro-musculo-skeltal system for human locomation, II. Real-time adaptability under various constraints. *Biological Cybernetics*, *73*, 113–121.

Taga, G. (1998). A model of the neuro-musculo-skeletal system for anticipatory adjustment of human locomotion during obstacle avoidance. *Biological Cybernetics*, *78*(1), 9–17.

Taga, G., Yamaguchi, Y., & Shimizu, H. (1991). Self-organized control of bipedal locomotion by neural oscillators in unpredictable environment. *Biological Cybernetics*, *65*(3), 147–159.

Takakusaki, K. (2017). Functional neuroanatomy for posture and gait control. *Journal of Movement Disorders*, *10*(1), 1.

Ting, L. H., Chiel, H. J., Trumbower, R. D., Allen, J. L., McKay, J. L., Hackney, M. E., & Kesar, T. M. (2015). Neuromechanical principles underlying movement modularity and their implications for rehabilitation. *Neuron*, *86*(1), 38–54.

Umberger, B. R., Gerritsen, K. G., & Martin, P. E. (2003). A model of human muscle energy expenditure. *Computer Methods in Biomechanics and Biomedical Engineering*, *6*(2), 99–111.

van der Kruk, E., & Geijtenbeek, T. (2023). A planar neuromuscular controller to simulate age-related adaptation strategies in the sit-to-walk movement. *bioRxiv*, 2023–11.

Winter, D. A. (1995). Human balance and posture control during standing and walking. *Gait & Posture*, *3*(4), 193–214.

Wolpert, D. M., & Kawato, M. (1998). Multiple paired forward and inverse models for motor control. *Neural Networks*, *11*(7–8), 1317–1329.

Wolpert, D. M., Miall, R. C., & Kawato, M. (1998). Internal models in the cerebellum. *Trends in Cognitive Sciences*, *2*(9), 338–347.

Zajac, F. E., Neptune, R. R., & Kautz, S. A. (2003). Biomechanics and muscle coordination of human walking: Part II: lessons from dynamical simulations and clinical implications. *Gait & Posture*, *17*(1), 1–17.

Zelik, K. E., & Adamczyk, P. G. (2016). A unified perspective on ankle push-off in human walking. *Journal of Experimental Biology*, *219*(23), 3676–3683.

Zhang, J., Fiers, P., Witte, K. A., Jackson, R. W., Poggensee, K. L., Atkeson, C. G., & Collins, S. H. (2017). Human-in-the-loop optimization of exoskeleton assistance during walking. *Science*, *356*(6344), 1280–1284.

Zych, M., Cannariato, A., Bonato, P., & Severini, G. (2021). Forward and backward walking share the same motor modules and locomotor adaptation strategies. *Heliyon*, *7*(8).